Title
Metallic Transition-Metal Dichalcogenide Nanocatalysts for Energy Conversion

Journal
Chem, 4(7)

ISSN
1925-6981

Authors
Li, Haoyi
Jia, Xiaofan
Zhang, Qi
et al.

Publication Date
2018-07-01

DOI
10.1016/j.chempr.2018.03.012

Peer reviewed

Chem

CellPress
REVIEWS

Review

Metallic Transition-Metal Dichalcogenide Nanocatalysts for Energy Conversion

Haoyi Li,[1] Xiaofan Jia,[2] Qi Zhang,[1] and Xun Wang[1,*]

Metallic transition-metal dichalcogenide (TMDC) nanomaterials have emerged as highly active and robust catalysts for energy conversion from renewable electricity or solar energy to fuels via electrochemical or solar-driven water-splitting technologies. Possessing intriguing electronic and catalytic properties, this category of materials based on earth-abundant elements is increasingly being explored and developed for practical applications. This review provides in-depth insights into recent progress regarding electrocatalysis and photocatalysis using metallic TMDC nanomaterials. After the introduction and fundamental illustration of the structures and extraordinary properties, we discuss the significant developments in synthetic methodologies and energy conversion applications with significant strategies for enhancing catalytic performance. Several personal perspectives on the opportunities and challenges in this promising realm are discussed in the conclusion.

INTRODUCTION

Sustainable and renewable energy sources have become increasingly indispensable because of the high demand for energy nowadays.[1] Hydrogen (H_2), regarded as a zero-carbon and clean-energy carrier with sufficient availability and high calorific value, has shown promise in meeting industrial and social requirements.[2] At present, the main sources of H_2 are reform reactions of hydrocarbons (such as methane) or alcohols (such as methanol) from natural gas, which have a low conversion rate and produce carbon dioxide (a potent greenhouse gas) as the by-product.[3] Therefore, it is worthwhile to explore and develop environmentally friendly and sustainable H_2 production technologies. The continued growth of renewable energy technologies has become significant on the basis of the fundamental demands of society to decrease the current reliance on fossil fuels.[4] Electrochemical and solar-driven water-splitting approaches are comparatively mature technologies for generating H_2, converting electric and photovoltaic energies to chemical fuels for storage and transport.[5,6] However, the noble-metal-based catalysts used in these technologies hinder their comprehensive development because of the high cost and scarcity.[7] Therefore, low-cost and earth-abundant alternatives with high activity and long-term durability are urgently required. Motivated by this extremely fascinating perspective, researchers have spared no efforts to develop innovative types of materials for energy conversion.

High-performance and inexpensive catalysts based on earth-abundant transition metals, such as hydroxides, oxides, sulfides, nitrides, phosphides, carbides, and selenides, have led to a breakthrough in the field of water-splitting technology.[8–14] Among these materials, transition-metal dichalcogenides (TMDCs) have been widely investigated because of their interesting physical, chemical, and electronic properties.[15–17] On the one hand, TMDC nanomaterials possess two-dimensional

The Bigger Picture

Comprehensive investigation of metallic transition-metal dichalcogenide (TMDC) nanocatalysts has surged in recent years because of their appealing electronic and catalytic properties. The excellent inherent catalytic activity makes these catalysts promising alternatives to noble-metal-based catalysts for facilitating energy conversion processes, especially for hydrogen evolution via electrochemical and solar-driven water splitting. The significant achievements can lead to sustainable energy conversion based on the large-scale deployment of earth-abundant catalysts.

This review focuses mainly on the progress in TMDC nanomaterials as catalysts for energy conversion. We demonstrate the key advances in synthetic methodologies and electrocatalytic and solar-driven water-splitting applications, especially innovative approaches to improving catalytic performance. The opportunities and challenges for the future development of metallic TMDC catalysts are also discussed.

(2D) layered structures just like graphene, which have the distinct feature of functioning at a thickness down to atomically thin mono- or multi-layers. The ultrathin nature of 2D TMDCs nanosheets contributes to the advantages of exposing catalytic active sites on both the edge and basal planes, which is beneficial for electrocatalysis and photocatalysis.[18,19] On the other hand, it is a universal principle that different electronic structures can give rise to changes in intrinsic catalytic activities.[20] Based on the achievements of various TMDCs, versatile electronic structures have been reported with diverse filling of the d orbitals of the transition metals, resulting in distinctive catalytic behavior. Except for selecting suitable TMDC compounds, the overall structural phase engineering is closely related to the changes in the electronic and crystal structures, which results in the formation of metallic and semiconducting phase TMDCs.[21] Compared with semiconducting phase TMDCs, metallic TMDCs with fascinating electronic structures can facilitate electrode kinetics, lower the loss of electrical transport, and increase the density of catalytic active sites, which enable the eye-catching enhancement of their intrinsic catalytic performance.[22] With the rapid development of this field, a large number of studies have been carried out on metallic TMDC nanomaterials in fundamental research and practical applications. From the perspective of the importance of catalysis using metallic TMDCs in strategic applications, this category of materials exhibit extraordinary advantages in contrast to other catalysts. Low-cost and accessible fabrication, as well as catalytic activity proximal to that of noble-metal-based catalysts, endow metallic TMDCs with promise and feasibility to be applied as state-of-the-art catalytic materials in practical water-splitting systems, and comparable catalytic performance to Pt-based catalysts has been shown in experimental measurements.[23] New members of this family of materials with innovatively designed architectures and corresponding facile synthetic processes are gradually being developed.

In this review, we mainly summarize recent progress in electrochemical and solar-driven water splitting utilizing metallic TMDC nanomaterials. First, we introduce the fundamental structures and extraordinary properties of this category of materials. Then, we provide in-depth insights into the synthetic methodologies, energy conversion applications, and relative mechanistic investigations to emphasize the key advances in promoting the catalytic performance of metallic TMDCs. Finally, we propose opportunities and challenges in this promising field to provide direction for future development.

FUNDAMENTAL STRUCTURAL FEATURES AND EXTRAORDINARY PROPERTIES

Generally, 2D TMDCs are denoted by the general formula MX_2, where M represents a transition-metal atom typically from group IVB to VIIB in the periodic table, and X is a chalcogen atom such as S, Se, or Te. In terms of molecular structure, these nanomaterials have the general form X–M–X, one unit of which is composed of three atomic layers. One metal atom layer in the center plane is sandwiched between two chalcogen atom layers, providing a stoichiometric ratio of 1/2 for MX_2.[24] In the compound molecule, +4 and −2 valence states correspond to the metal and chalcogen atoms, respectively. The valence states of the elements reflect the degree of oxidation, further affecting the strength of the ionic bonds between transition-metal and chalcogen atoms.[21] In the interlayer of 2D TMDCs, there are weak van der Waals forces, leading to the formation of single layers from the bulk counterpart via exfoliation.[25] According to the structure of the unit cell, the phase of TMDCs is classified as trigonal prismatic and octahedral (Figure 1A).[24] The trigonal prismatic phase matches the 2H or 3R phase, which has the same metal atom coordination

[1]Key Lab of Organic Optoelectronics and Molecular Engineering, Department of Chemistry, Tsinghua University, Beijing 100084, China

[2]Department of Chemistry, University of Virginia, Charlottesville, VA 22904, USA

*Correspondence:
wangxun@mail.tsinghua.edu.cn

https://doi.org/10.1016/j.chempr.2018.03.012

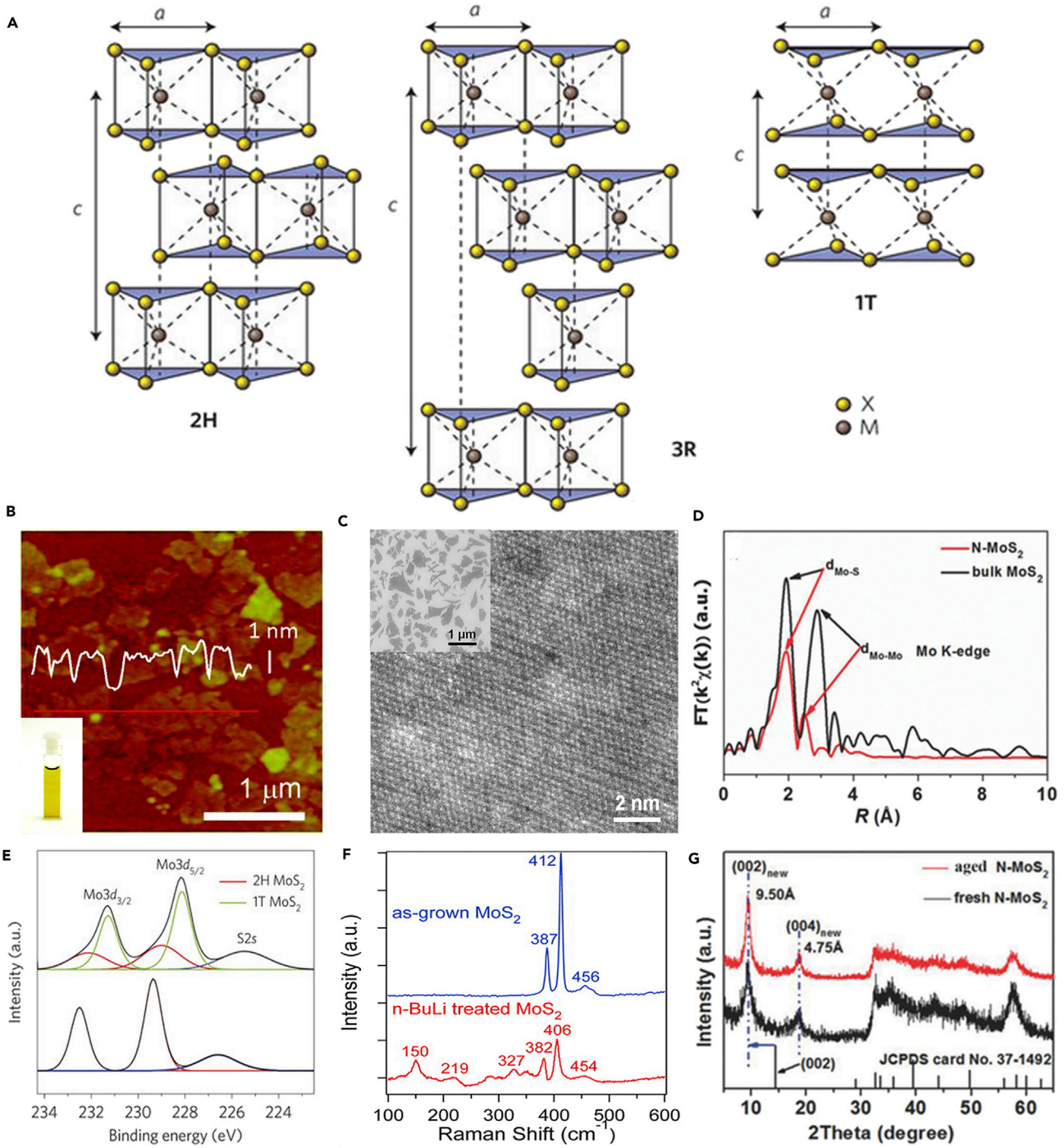

Figure 1. Fundamental Structures and Distinctive Characteristics of Metallic TMDCs

(A) The structure polymorphs of TMDCs: 2H, 3R, and 1T. The yellow ball represents a chalcogen atom (X), and the gray ball represents a transition-metal atom (M). Reprinted by permission from Springer Customer Service Centre GmbH: Springer Nature, *Nature Nanotechnology* Wang et al.,[24] copyright 2012.

(B) A large-scale atomic force microscopy (AFM) image of exfoliated MoS_2 flakes. The white line is the height measurement taken from the red line. The inset shows a typical digital photo of lithium-intercalated and exfoliated MoS_2 suspension in water. Reprinted with permission from Eda et al.[26] Copyright 2011 American Chemical Society.

(C) HRSTEM image of a metallic 1T MoS_2 nanosheet obtained by chemical exfoliation. Inset: SEM image of the corresponding products showing large-scale production. Reprinted with permission from Voiry et al.[27] Copyright 2013 American Chemical Society.

Figure 1. *Continued*

(D) FT analyses at Mo K-edge in R-space from EXAFS data reveal shortening of the Mo–Mo bond length and Mo–S coordination state in metallic 1T MoS_2 in contrast with the bulk sample (2H phase). Reprinted with permission from Liu et al.[28] Copyright 2015 Wiley-VCH Verlag GmbH & Co. KGaA.

(E) XPS spectra showing the Mo 3d and S 2s regions of 1T and 2H phase MoS_2. The lower curve corresponds to a typical 2H phase, and the upper curve can be fitted with both 1T and 2H phase components. Reprinted by permission from Springer Customer Service Centre GmbH: Springer Nature, *Nature Materials* Kappera et al.,[25] copyright 2014.

(F) Raman spectra comparing the as-grown sample (2H phase) and the exfoliated MoS_2 (1T phase) nanosheets. Reprinted with permission from Lukowski et al.[29] Copyright 2013 American Chemical Society.

(G) XRD patterns of metallic 1T MoS_2 nanosheets, including fresh and 6-month-old samples. The shift of the (002) peak exhibits increasing interlayer distance compared with that of the JCPDS card for 2H phase MoS_2. Reprinted with permission from Liu et al.[28] Copyright 2015 Wiley-VCH Verlag GmbH & Co. KGaA.

and can be distinguished from symmetry. The two X–M–X layers of one unit cell in 2H phase TMDCs exhibit a hexagonal symmetry of stacking belonging to the D_{3h} group and the three X–M–X layers of one unit cell in 3R phase display a rhombohedral symmetry of stacking affiliated to the C_{3v} group. Meanwhile, the octahedral phase refers to the 1T phase, which has the characteristics of tetragonal symmetry (D_{3d} group) and octahedral coordination of the metal atoms. Different phases vary the electronic structures because of diverse filling of the d orbitals of the transition metal. Combined with energy band structures, their semiconducting nature is attributed to the fully filled d orbitals, whereas partially filled d orbitals cause their metallic nature.[21] Some TMDCs in a thermodynamic stable state have semiconducting properties (such as MoX_2, WX_2, and ReX_2), and others show metallic features (such as TiX_2, VX_2, NbX_2, and TaX_2).[30,31]

For metallic TMDCs, there are a few distinctive characteristics that distinguish them from their pristine semiconducting counterparts. As shown in Figure 1B, metallic 1T MoS_2 produced via lithium intercalation and exfoliation shows large-sized ultrathin flakes of 1–1.2 nm thickness in solution phase.[26] A high-resolution scanning transmission electron microscopy (HRSTEM) image (Figure 1C) shows the distorted regions with zigzag chains of Mo clusters and (2a × a) superlattices,[27] which mostly belong to WTe_2-type structures, with a minority matching undistorted TiS_2-like structures.[32,33] The WTe_2-type structures of metallic TMDCs are special forms of ideal metallic phase structures, denoted as 1T′ phase for MoX_2 and WX_2. A scanning electron microscopy (SEM) image of the large-scale production of exfoliated MoS_2 nanosheets is displayed in the inset of Figure 1C. The Fourier-transform (FT) profiles (Figure 1D) at the Mo K-edge in R space from synchrotron radiation-based extended X-ray absorption fine structure (EXAFS) data reveal an obvious shift from 3.18 to 2.75 Å of the second peaks related to the Mo–Mo bond at the near edge. Phase transition from 2H to 1T phase gives rise to shortening of the Mo–Mo bond of MoS_2. The peak intensity of the nearest Mo–Mo bond decreases, suggesting a reduction in the coordination number of Mo–Mo. This changes demonstrate that 1T MoS_2 is appropriate for distorted octahedral coordination.[28] In addition, X-ray photoelectron spectroscopy (XPS) also provides direct evidence for differentiating metallic 1T and semiconducting 2H phase TMDCs. This measurement is sensitive to changes in the Fermi level between phases 1T and 2H.[34] Compared with 2H phase, the peak positions of metal orbitals in 1T phase have an evident downshift of about 0.8 eV (Figure 1E).[25] It is not easy to identify the ideal undistorted or distorted structures of 1T phase from XPS spectra. Raman shifts at 150, 219, and 327 cm^{-1} (recorded as J_1, J_2, and J_3, respectively), except for the E_{2g} and A_{1g} modes of pristine 2H MoS_2 (Figure 1F), testify to the formation of 1T MoS_2,[35] which corresponds to the superlattice structure of the distorted 1T phase.[29] Intercalation may lead to enlargement of the interlayer spacing of TMDCs, which can be demonstrated by X-ray diffraction (XRD) from the shifted peak of the layer.[28] In Figure 1G, the (002) peak of 1T MoS_2 downshifts to a lower degree of 9.31°, and a new (004) peak at 18.65°

also appears. Compared with pristine MoS_2, (the (002) peak is located at 14.38°, corresponding to interlayer spacing of 6.15 Å), the interlayer spacing of 1T MoS_2 is increased by 3.35 Å, indicating the existence of intercalant in the interlayer. These distinctive characteristics can assist in identifying the formation of metallic TMDCs, in favor of further practical applications.

With regard to energy conversion-related electro- and photocatalysis, semiconducting TMDCs do not give a high performance because of the slower charge-transfer kinetics and passivated active sites.[27,36] Compared with their semiconducting counterparts, metallic TMDCs show extraordinarily interesting properties for catalysis. The band gap of TMDC can be tuned by phase engineering,[20,21,24] which means the electrical conductivity of TMDC enables remarkable enhancement from semiconducting to metallic characteristics. This feature is considered pivotal for improving catalytic performance. Metallic TMDCs are endowed with faster electrode kinetics and lower loss of electrical transport during electrocatalysis.[22] Moreover, it has been proven that the inherent catalytic activities of metallic TMDCs are much higher than semiconducting TMDCs as a result of the proliferated active sites.[27,37] In contrast to the inert basal planes of semiconducting TMDCs, metallic TMDCs are catalytically active at both basal planes and edges and possess thermoneutral hydrogen adsorption free energy benefitting the hydrogen evolution reaction (HER). Conversion of semiconducting TMDCs to their metallic counterparts through structural phase transition is a great success, and enhancement of catalytic activity can be easily achieved. The key advances of metallic TMDC nanomaterials in energy conversion-related catalysis emphasized here have core significance for utilization in practical water-splitting systems.

SYNTHETIC METHODOLOGIES

High-quality target product prepared by an accessible synthetic methodology is a basic requirement for investigating the properties and practical applications. In this section, we summarize the available synthetic strategies for metallic TMDC nanomaterials, including top-down exfoliation from bulk counterparts, bottom-up direct synthesis, and other alternative approaches inducing phase transition. We also evaluate the relative advantages and weaknesses of each specific strategy.

Top-Down Synthesis via Exfoliation with Alkali Metal Intercalation

At present, the most commonly used strategy for synthesizing metallic Mo or W chalcogenide nanomaterials is exfoliation assisted by organolithium intercalation from semiconducting counterparts. As a reducing agent, organolithium can donate an electron to TMDCs, which is transferred into the d orbital of the transition metal and thus increases the electron density. This electron transfer process may induce phase transition from hexagonal phase to tetragonal phase. On the basis of this method, high-quality and large-sized 2D metallic TMDCs nanosheets were easily produced (Figure 1C) and utilized in HER for energy conversion.[26,27,29,38,39] Typically, mono- or multi-layer TMDC nanosheets were produced via the intercalation of Li^+ by soaking counterpart powders in a hexane solution of n-butyl lithium for 48 hr and subsequent reaction between the intermediate product with water. During the process of intercalation and exfoliation, microwave and ultrasonication can be used to induce slippage between flakes, facilitating the infiltration of lithium ions.[40] Moreover, the lithiation approach can also be applied to induce phase transition from 1T to 2H phase of TaS_2; the 1T phase is thermodynamically stable.[41] This strategy for manufacturing metallic TMDCs is quite facile to acquire pure phase, high-quality, and monolayer 2D TMDC nanosheets with large flake size. Nevertheless, it is still a

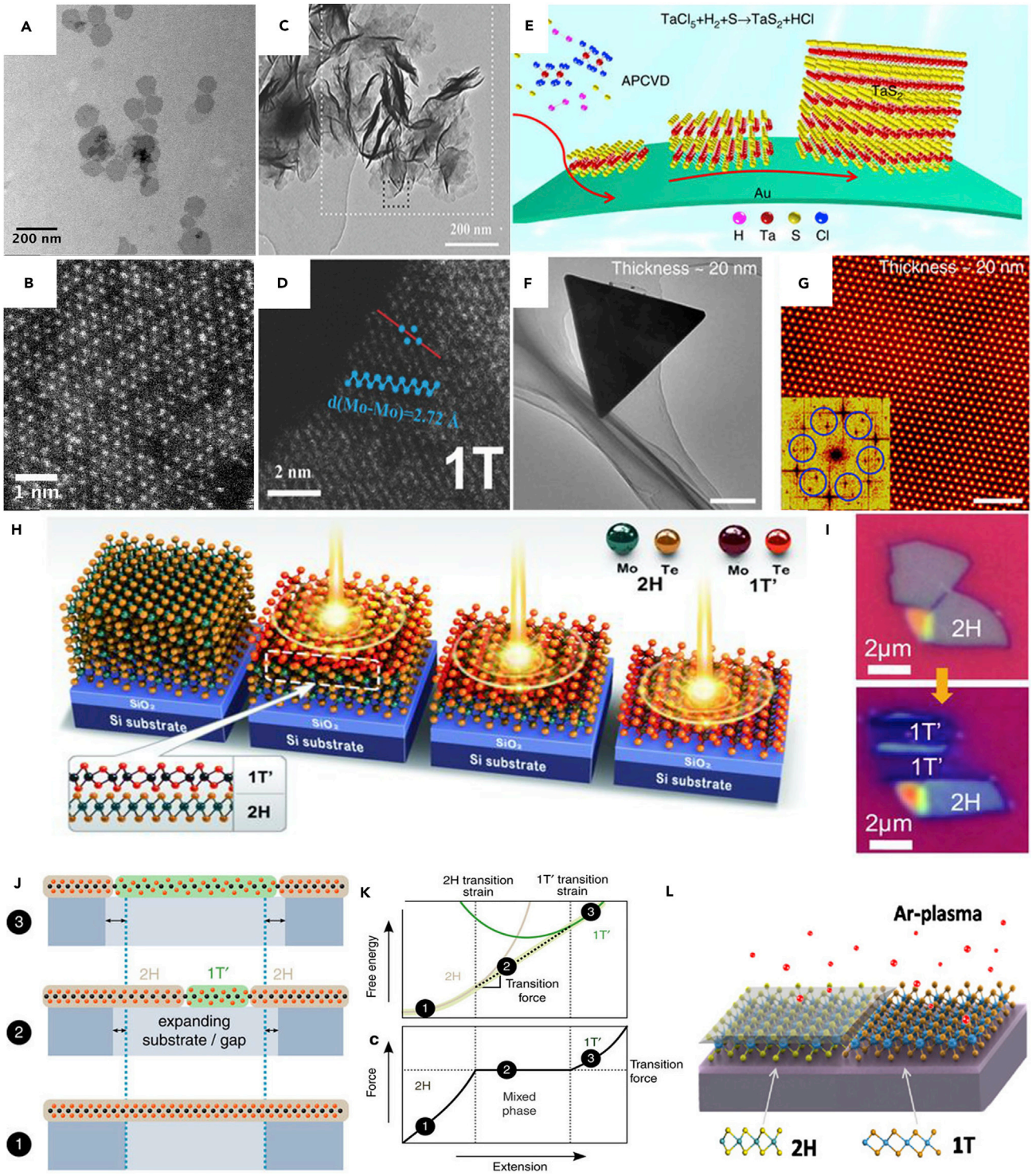

Figure 2. Diverse Strategies for Synthesis of Metallic TMDCs

(A and B) TEM (A) and HRSTEM (B) images of 1T WS_2 nanosheets via colloidal synthesis. Reprinted with permission from Mahler et al.[48] Copyright 2014 American Chemical Society.

(C and D) TEM (C) and HRSTEM (D) images of 1T MoS_2 nanosheets via hydrothermal reaction. Reprinted with permission from Liu et al.[28] Copyright 2015 Wiley-VCH Verlag GmbH & Co. KGaA.

(E) Schematic illustration of APCVD growth for metallic TaS_2. Reprinted from Shi et al.[51]

Figure 2. *Continued*

(F and G) TEM (F) and HRSTEM (G) images exhibit a triangle domain of 2H TaS_2 with thickness of ~20 nm and disordered periodic lattice distortion with hexagonal symmetry. Inset in (G) is the corresponding FFT pattern. Scale bars, (F) 1 μm and (G) 3 nm. Reprinted from Shi et al.[51]

(H and I) Schematic illustration of the laser-irradiation process for phase patterning of $MoTe_2$ (H) and optical microscopy images of exfoliated 2H $MoTe_2$ flakes before (upper) and after (lower) laser irradiation. Patterned and nonpatterned areas are marked by 1T′ and 2H, respectively. Reprinted with permission from Cho et al.[52] Copyright 2015 AAAS.

(J) Schematic diagram exhibiting the phase transition from 2H to 1T of single-layer TMDCs via uniaxial strain. The region can be freely suspended or located on a low-friction substrate. Reprinted by permission from Springer Customer Service Centre GmbH: Springer Nature, *Nature Communications* Duerloo et al.,[53] copyright 2014.

(K) The relationship of Helmholtz free energy and force with degree of deformation. In step 1, only 2H phase deformation exists, and no phase transition is observed. In step 2, the lowest free-energy path is a common tangent between the 2H and 1T′ energy surfaces, indicating co-existence of the two phases. A plateau of the external force is shown in this domain. In step 3, further extension may cause the complete phase transformation to 1T′ phase. Reprinted by permission from Springer Customer Service Centre GmbH: Springer Nature, *Nature Communications* Duerloo et al.,[53] copyright 2014.

(L) Schematic formation of 1T MoS_2 through Ar plasma treatment. Reprinted with permission from Zhu et al.[54] Copyright 2017 American Chemical Society.

great challenge to improve the yield via this method, which reaches just 10%–20%. The metastable feature of the products,[42] meaning that the metallic TMDCs are readily converted back to semiconducting phase, especially for MoS_2, should also be considered. The nonuniformity of the size and morphology is another issue to be addressed. Therefore, there is still a long way to go to improve this strategy.

Some further developments based on this strategy have been explored. (1) Electrochemical intercalation: Zhang and co-workers previously reported lithium intercalation of TMDCs via an electrochemical method. Single-layer MoS_2, WS_2, TiS_2, TaS_2, ZrS_2, $NbSe_2$, etc. have been successfully synthesized and gaseous by-products enabled the separation of the nanosheets.[43,44] (2) Solid-state intercalation: using lithium borohydride can result in intercalated TMDCs powders (such as ReS_2 and WS_2) at a high temperature.[45,46] (3) Changing reducing agent and intercalated ions: Zheng and co-workers used naphthalenide as the reducing agent instead of butyl and other alkali metals as intercalated ions to realize the high-efficiency intercalation and exfoliation of TMDCs.[47] Although there are still numerous efforts that need to be explored, these are not discussed here. Instead, we discuss the possibilities for future development.

Bottom-Up Direct Synthesis

In contrast to top-down exfoliation, bottom-up direct synthesis has the advantages of high-purity and high-quality production, rapid reaction, uniform product size and morphology, and simple operation. These superiorities endow these strategies with a higher possibility for practical use. In this section, we introduce colloidal synthesis and chemical vapor deposition (CVD) methods.

Colloidal synthesis can successfully achieve comparatively large-scale production with high quality. Colloidal synthesis may improve the stability of metastable metallic TMDCs via the introduction of interactional substances,[28,48] which is an advantage over the intercalation-exfoliation strategy. In recent years, this method has facilitated extension of reaction systems for the synthesis of various metallic TMDCs. Mahler et al.[48] have studied the colloidal synthetic protocol for producing WS_2 monolayers in an oleophilic reaction system. As shown in Figures 2A and 2B, the as-prepared 1T WS_2 presents a monodisperse rounded nanosheet morphology with a diameter of ~100 nm and a typical distorted 1T structure. In this system, the phase transition of WS_2 can be realized by a slight modification of the reaction conditions, which provides an opportunity to develop controllable synthesis for phase engineering of colloidal TMDCs. A facile one-step hydrothermal reaction can also realize production of colloidal 1T MoS_2.[28] The ultrathin nature of the nanosheets and highly

distorted octahedral structure with (2a × a) superlattice regions confirm the formation of 1T MoS_2 (Figures 2C and 2D). Moreover, multi-layer 1T′ $MoTe_2$ and $MoSe_2$ nanosheets were successfully synthesized via a one-pot solvothermal strategy,[49,50] enriching the family of colloidal synthetic strategies for metallic TMDCs. However, there are still some issues to be addressed for colloidal synthesis in future studies, such as the selection of reaction systems, environmental impacts, and product repeatability. We believe that colloidal synthesis will become one of the most essential methodologies in practical applications.

The key advances with CVD synthesis are high-quality products with a clean surface and uniform size and morphology, which facilitates investigation of the detailed atomic structures and electronic properties of the materials. Here, we emphasize fabrication of metallic TaS_2 and VS_2. Low and atmospheric pressure CVD (LPCVD and APCVD) routes have been designed by Shi et al.[51] to directly synthesize metallic centimeter-sized uniform, ultrathin TaS_2 films and thickness-tunable TaS_2 flakes on Au foil (Figures 2E and 2F). The highly crystalline TaS_2 with a hexagonally arranged Bragg scattering pattern displays the single-crystalline feature of the 2H TaS_2 triangle (Figure 2G). Similarly, Ji et al.[55] reported an APCVD method for the growth of metallic VS_2 nanosheets on SiO_2/Si substrate with sub-10 nm thickness and lateral sizes of tens of micrometers. These studies are extremely pioneering for CVD growth of metallic TMDCs. More efforts should be made to expand the family of compounds obtained by this route. The disadvantages of CVD synthesis, such as high cost, high energy consumption, and relatively small-scale production, hinder the rapid development and scale-up applications, and thus other efficient designs still need to be explored.

Other Alternative Strategies for Phase Transition

Several strategies have also driven endeavors to bring about phase transition of TMDCs. Here, we summarize some typical and fascinating examples. (1) Laser-induced: an ohmic heterophase homojunction between 2H and 1T′ $MoTe_2$ has been fabricated using a laser-induced phase patterning method (Figure 2H).[52] Figure 2I shows that the $MoTe_2$ flakes become thinner and a new structural phase evolves after laser irradiation. (2) Mechanical strain: a freely suspended TMDC monolayer with its armchair axis pointing across a trench is shown in Figure 2J, which requires a range of tensile strains from 0.3% to 3% for phase transition under uniaxial conditions.[53] The Helmholtz free energy and force changes along with the degree of deformation are shown in Figure 2K. (3) Weak Ar-plasma treatment: Zhu and coworkers utilized weak Ar-plasma bombardment to locally induce phase transition from 2H to 1T monolayer MoS_2 to form mosaic structures (Figure 2L).[54] Lateral sliding of the top S layer is triggered by kinetic energy from Ar ions (in plasma), which leads to the generation of 1T phase nanostructures. In addition, electron beam irradiation[56] and hot electrons generated from plasmon decay[57] can also motivate phase transition of MoS_2 from 2H to 1T phase. It is believed that these latest routes to thermodynamically impel phase transitions between semiconducting and metallic-group VIB TMDCs hold great promise for future studies.

STABILITY OF METALLIC TMDC NANOMATERIALS

In this section, we discuss strategies for stabilizing metallic-group VIB TMDCs given that very few reports are related to the stability of other metallic TMDCs. This feature plays an essential role in fundamental research and practical applications. Structural stability is considered to be one of the most important issues that need to be urgently addressed to achieve widespread use in future applications. It is widely proven that semiconducting VIB TMDCs are thermodynamically stable, whereas the metallic 1T

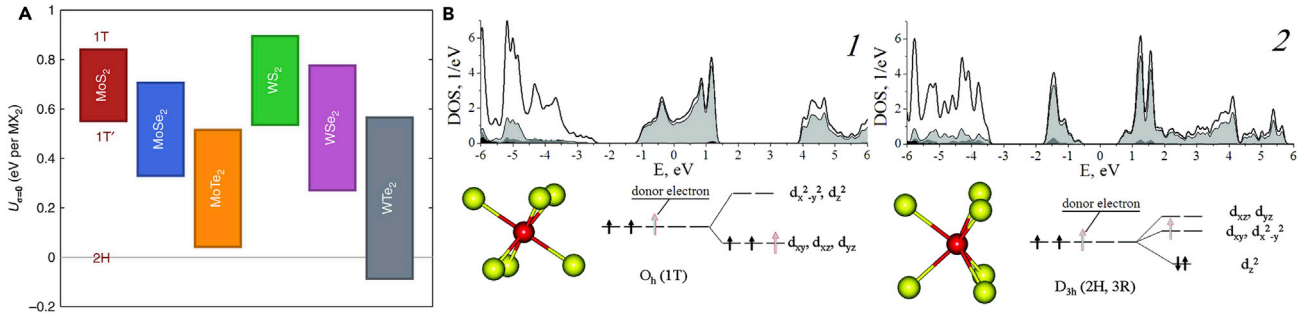

Figure 3. Stability-Related Calculations of Metallic Group VIB TMDCs

(A) Differences in phase energetics among 2H, 1T, and 1T′ group VIB TMDCs without mechanical stress. Reprinted by permission from Springer Customer Service Centre GmbH: Springer Nature, *Nature Communications* Duerloo et al.,[53] copyright 2014.

(B) Mo 4d densities of state (DOS) and simplified illustrations within crystal field theory for 1T (1) and 2H MoS_2 (2). Fermi level is set to 0 eV. For 2H MoS_2, the Fermi level passes through the band gap and is semiconducting. For 1T MoS_2, a wide band hosts the Fermi level and thus it is metallic. By doping the 1T MoS_2 lattice with a donor electron, the Mo $4d_{xy,yz,xz}$ orbitals become half-filled and thus the 1T phase is stabilized. On the contrary, when electrons are donated to the Mo $4d_{xy}$ orbitals of 2H MoS_2 and the Mo $4d_{x2-y2}$ orbitals remain unoccupied, the electronic structure has metallic character, which leads to destabilization of the lattice. Reprinted with permission from Enyashin et al.[60] Copyright 2011 American Chemical Society.

phase is metastable and is preferentially converted back to 2H phase.[58] Some investigations have been carried out to develop effective ways and prove that it is quite possible to realize the stability of metallic-group VIB TMDCs. The fundamental influences on the structural stability of 1T phase are structural distortion and the existence of interacting matter.[21,53] As shown in Figure 3A, the 1T′ phase MX_2 has much lower ground-state energy without mechanical stress than that of 1T phase counterparts. Coupled with mechanical strain, the structural deformation can be tuned to achieve different levels of phase transition, and thus the stability of metallic TMDCs depends on the structural distortion.[53,59] Furthermore, introducing interacting matter can drastically enhance the structural stability of metallic TMDCs. Ammonium ions[28] and surface ligands[48] can interact with MoS_2^- and WS_2^- forming electrostatic forces that benefit stabilization. Meanwhile, the electro-donating character of Au or Re impurities makes 1T phase MoS_2 and WS_2 genuinely more stable.[56,57,60] Electron donation of Mo d_{xy} levels has been shown to stabilize 1T phase and destabilize 2H phase (Figure 3B). Negative charges can also affect the stabilization of metallic TMDCs. Excess charges in 1T MoS_2 and WS_2 keep the higher temperatures of 1T-to-2H phase transition, but charge reduction by halogen induction decreases the temperatures.[32,46] According to first principles calculations, there is an energy barrier of 0.95 eV for 1T to 2H phase transition, which agrees with the experimental measurement value of ~0.87 eV.[39,46] These results indicate that the stability of metallic TMDCs is realizable. The structural stabilization of metallic TMDCs as electrode materials during electrolysis is the basis of practical utilization. Our previous work[61] verified that amorphous Ni–Co complexes can stabilize 1T MoS_2 under external oxidation potentials; we propose that the reason for this is that the strain generated by the amorphous part makes the structure of 1T MoS_2 distorted. Notably, a single-walled carbon nanotube is an excellent choice for hybridization with metallic TMDCs (e.g., MoS_2[62] and $MoSe_2$[63]), which significantly benefits a high-efficiency electron/ion transport pathway and structural stability. Hybridization may provide a potential opportunity to realize feasible industrial and social deployment of metallic TMDCs.

UTILIZING METALLIC TMDC NANOMATERIALS AS CATALYSTS FOR ENERGY CONVERSION

High-efficiency and ultrastable catalysts for energy conversion hold tremendous promise for industrial deployment and social demands. Here, we mainly focus on

hydrogen generation through electrocatalytic and solar-driven water splitting, which has attracted a great deal of attention in recent years. The major aim of most studies is to develop low-cost and earth-abundant alternatives to noble-metal-based catalysts with high activity and long-term durability. Metallic TMDCs, a novel category of catalysts based on non-noble metals, possess fascinating catalytic activities for hydrogen production, making a momentous contribution to sustainable development of energy utilization and environmental pollution control. Their structural and electronic properties can be tuned to explore the fundamental behavior and enhance catalytic performance. In this section, we present recent progress in metallic TMDCs for electrocatalysis and photocatalysis and present some related mechanistic examples to clarify the world of the catalytic HER over metallic TMDCs.

Metallic TMDCs for HER Electrocatalysis

Electrochemical HER from water splitting is an effective and environmentally friendly way to produce hydrogen.[6] Compared with their semiconducting counterparts, metallic TMDCs as highly active and robust electrocatalysts are predominate in intrinsic catalytic activity because of their distinctive structural and electronic structures. To be specific, proliferative catalytically active sites and fast electrode kinetics and charge transport are the two core advantages of metallic TMDCs in electrocatalysis. We further demonstrate the underlying reasons for the inherent superiorities and structural and compositional designs for the enhanced performance. Other factors influencing HER activities on the basis of metallic TMDCs are also proposed.

Identification of the Intrinsic Electrocatalytic Activity

MoS_2 is one of the most studied TMDCs and the most promising candidates for HER electrocatalysis to replace Pt-based noble-metal materials for practical applications.[15,16,22] In 2005, Hinnemann and co-workers first proved the presence of electrocatalytic active sites for HER located on the edges of MoS_2 nanoparticles by density functional theory (DFT) calculations.[64] Figure 4A shows the sulfur sites of hydrogen binding at the edges are 2-fold coordinated to molybdenum atoms. According to the calculations, the first hydrogen is strongly bound and additional hydrogen atoms are adsorbed with a low barrier on the edges, and the hydrogen coverage increases from 25% to 50%. The results theoretically identify MoS_2 as a promising electrocatalyst for HER. By 2007, Jaramillo et al.[65] had first performed experiments to show that the sulfided Mo edges are active for HER. The exchange current density was plotted against the MoS_2 area coverage (Figure 4B) and the MoS_2 edge length (Figure 4C). The data points have a linear relationship only when plotted versus edge length. Therefore, the activity on the edges of MoS_2 for HER has been proved. However, the above demonstration is suitable only for semiconducting 2H MoS_2, which suggests that the basal plane of 2H MoS_2 is catalytically inactive.

On the contrary, metallic MoS_2 possesses active sites for HER on both the basal plane and the edges of the layered grains and, compared with 2H MoS_2, has a proliferation of catalytic active sites. According to the lower ground-state energy of 1T′ MoS_2 (Figure 3A), the 1T phase preferentially transforms back to the more stable 2H and 1T′ phase thermodynamically.[53] During the HER, 1T′ MoS_2 tends to be found rather than 1T phase, and it is proved to be the most active polytype for HER.[66] The probable sites of hydrogen adsorption on the surface of single-layer MoS_2 are marked by numbers in Figure 4D, and the corresponding Gibbs free energy (ΔG_{H^*}) of the first and second hydrogen binding on the surface of 1H (single-layer 2H phase), 1T, and 1T′ MoS_2 via DFT calculations are presented in Table 1. The most available behavior of HER catalysis requires $\Delta G \cong 0$ because if hydrogen binds

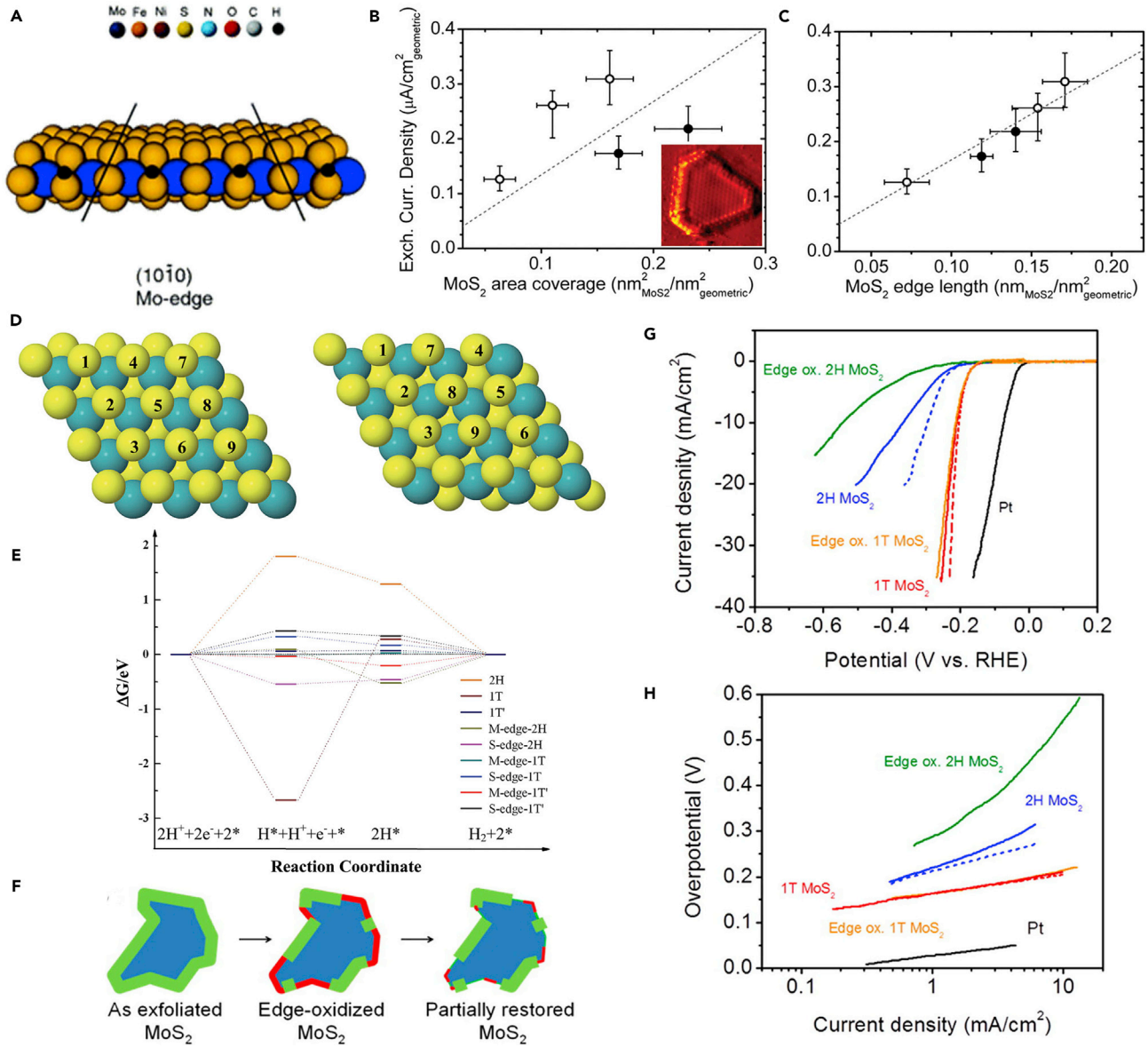

Figure 4. Identifications of Electrocatalytic Active Sites in MoS_2 Polymorphs for HER

(A) Schematic representation of the (10$\bar{1}$0) Mo-edge. The hydrogen binds at every second sulfur atom. The *x* direction in the unit cell is marked by the two lines. Reprinted with permission from Hinnemann et al.[64] Copyright 2005 American Chemical Society.

(B and C) Exchange current density versus MoS_2 area coverage (B) and edge length (C). The exchange current density does not correlate with the area coverage of MoS_2, whereas it has a linear relationship with the MoS_2 edge length. Inset in (B): atomically resolved scanning tunneling microscope (STM) image of MoS_2 showing the predominance of the sulfided Mo-edge. Reprinted with permission from Jaramillo et al.[65] Copyright 2007 AAAS.

(D and E) Scheme of the supercells showing the sites of hydrogen adsorption on the surface of 1H and 1T MoS_2 (left) and 1T′ MoS_2 (right) (D) and Gibbs free energy of HER at the basal planes and edges of 1H, 1T, and 1T′ MoS_2 calculated by DFT (E). Reproduced from Fan et al.[66] with permission of the Royal Society of Chemistry.

(F–H) Schematic illustration of the oxidation process and partial restoration of the MoS_2 nanosheet edges (F) and polarization curves (G) and corresponding Tafel plots (H) of 1T and 2H MoS_2 nanosheets before and after edge oxidation for HER. iR correction was performed and is shown by the dashed lines. Tafel slopes of ~40 and 75–85 mV/decade indicate the HER kinetics for 1T and 2H MoS_2, respectively. After oxidation, the values increase to 45 and 186 mV/decade. Reprinted with permission from Voiry et al.[27] Copyright 2013 American Chemical Society.

too weakly, the production of surface H* (adsorbed hydrogen) is hampered; if hydrogen binds too strongly, it is quite difficult for H* to produce H_2. Comparing the values in Table 1, it is believed that the basal plane of 1T′ MoS_2 has the main

Table 1. Evidence of Active Sites on the Basal Plane of MoS_2 Polymorphs for HER via Gibbs Free Energy

	$\Delta G^{H1}{}_1$ (eV)	$\Delta G^{H2}{}_1$ (eV)				
	Site 1	Sites 1 and 2	Sites 1 and 3	Sites 1 and 5	Sites 1 and 6	Sites 1 and 8
1H MoS_2	1.8	1.29	1.5	1.37	1.54	1.51
1T MoS_2	−2.67	0.63	0.63	0.28	0.60	0.69
1T′ MoS_2	0.06 (0.73[a])	0.22	0.20	0.11	0.07	0.85[a]

Gibbs free energy of the first and second hydrogen bindings on the surface of 1H, 1T, and 1T′ MoS_2 via DFT calculations. The first H adsorbs on site 1, and the second H adsorbs on sites 2, 3, 5, 6, and 8. Reproduced from Fan et al.[66] with permission of the Royal Society of Chemistry.

[a]The values of Gibbs free energy on the high S atom.

active sites for HER. The metal edges of 1T and 1T′ MoS_2 exhibit near-zero ΔG_{H^*} values compared with the higher values of 1H MoS_2 according to the calculation results (Figure 4E), which indicates that the metal edges of 1T and 1T′ MoS_2 are also extraordinarily active. Moreover, Voiry et al.[27] achieved the synthesis of edge-oxidized metallic MoS_2 (Figure 4F) and measured HER electrocatalytic activity (Figures 4G and 4H). It can be observed that there is negligible degradation of the HER activity on edge-oxidized metallic MoS_2 compared with pristine 1T MoS_2. This experimental result clarifies that the active sites on metallic MoS_2 are located at both the basal planes and the edges. Similarly, this new phenomenon is appropriate for other metallic TMDCs and at this point, evidence of the active sites of entire nanostructures in metallic TMDCs has been established.[38,50,51]

According to the Sabatier principle, moderate binding energies of hydrogen adsorption are optimal for HER.[22,65] As shown in the volcano plot (Figure 5A), ΔG_{H^*} of MoS_2 electrocatalysts approach a thermoneutral state and the exchange current densities are located below the Pt-group metals, which means that MoS_2 has great potential to act as a highly efficient electrocatalyst for HER. Estimation of the catalytic activity and stability for HER based on the hydrogen adsorption process from DFT calculations can be expanded to all kinds of transition-metal disulfides and diselenides.[37] Figures 5B and 5C elucidate the relationship between H–X (X = S or Se) adsorption free energy (ΔG_{HX}) and hydrogen binding free energy (ΔG_H) for semiconducting and metallic TMDCs. The increasing tendency of activity matches the thermoneutral value of ΔG_H, and a more stable catalyst needs stronger H–X binding ($\Delta G_{HX} < 0$), which is adverse to desorption of HX as H_2X. In contrast to semiconducting TMDCs, metallic TMDCs possess lower values of ΔG_H and ΔG_{HX} integrally and different trends for sulfides and selenides, indicating higher stability and activity in metallic TMDCs. These results indicate the intrinsic high performance of metallic TMDCs for HER theoretically. Among the superior electrocatalysts, some have been explored for practical HER catalysis. We choose three typical examples synthesized via different strategies to demonstrate the splendid electrocatalytic behaviors. First, Shi et al.[51] reported that excellent performance for HER approaching that of commercial Pt was established directly by CVD-grown metallic 2H TaS_2 (Figure 5D). Various polarization abilities were achieved with 2H TaS_2 flakes of different thickness, and the best performance, 65mV of overpotential affording a cathodic current density of 10 mA cm^{-2}, was produced by flakes 150 nm thick (Figure 5E). Furthermore, fast electrode kinetics (~33 mV/decade) and low charge-transfer resistance (~5 Ω) were exhibited in Tafel plots (Figure 5F) and Nyquist plots of electrochemical impedance (Figure 5G), which were attributed to the metallic nature of the catalyst. The experimental measurements verify the distinctive advantage of metallic TMDCs, markedly enhanced conductivity, over their semiconducting

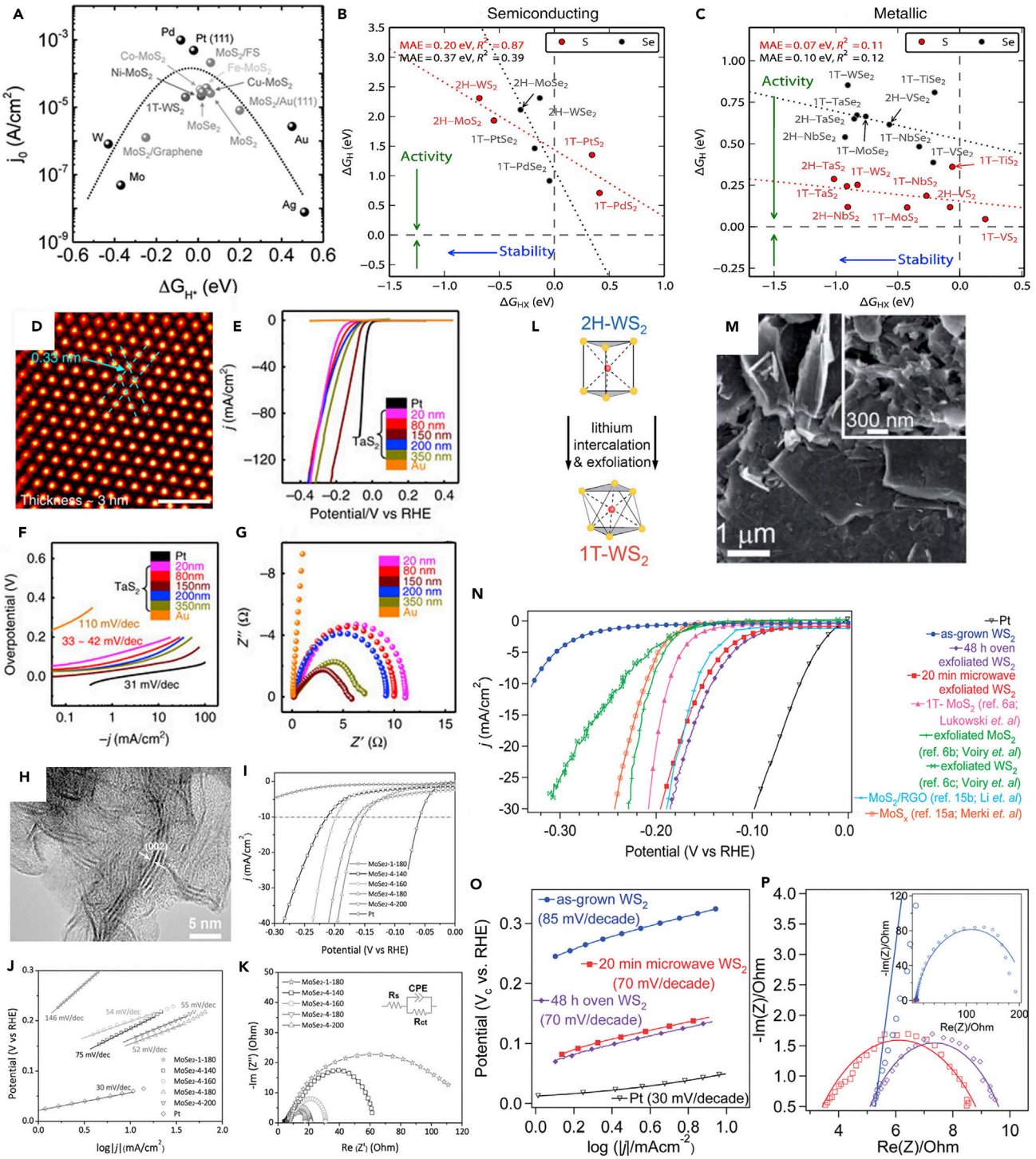

Figure 5. Thermodynamics of Hydrogen Adsorption on 2D TMDCs and Corresponding Electrocatalytic Examples

(A) Volcano plot showing the relationship between exchange current density and the DFT-calculated Gibbs free energies of adsorbed atomic hydrogen. Reprinted with permission from Voiry et al.[22] Copyright 2016 Wiley-VCH Verlag GmbH & Co. KGaA.

(B and C) The inverse linear relationship between ΔG_{H^*} and ΔG_{HX} for semiconducting (B) and metallic (C) TMDCs. These plots generally indicate that more reactive and stable TMDCs lead to stronger X binding and weaker H binding. Reprinted from Tsai et al.[37]

Figure 5. *Continued*

(D–G) Atomic-resolution TEM image of the as-grown 2H TaS_2 by CVD (scale bar, 1 nm) (D) and polarization curves (iR corrected) (E), corresponding Tafel plots (F), and Nyquist plots (G) exhibiting electrochemical impedance of as-synthesized 2H TaS_2 with different thicknesses, compared with Au substrate and commercial Pt. Reprinted from Shi et al.[51]

(H–K) HRTEM image of as-prepared 1T $MoSe_2$ nanosheets (H) and polarization curves (iR corrected) (I), corresponding Tafel plots (J), and Nyquist plots (K) showing electrochemical impedance of as-synthesized 1T $MoSe_2$ produced under different conditions than commercial Pt. Reprinted with permission from Yin et al.[50] Copyright 2017 Wiley-VCH Verlag GmbH & Co. KGaA.

(L–P) Schematic representation of 2H-to-1T phase transition of as-synthesized WS_2 nanosheets via chemical exfoliation (L), SEM image of 1T WS_2 nanosheets supported on graphite (inset shows 1T WS_2 nanosheets with a large quantity of exposed edges) (M), and polarization curves (iR corrected) (N), corresponding Tafel plots (O), and Nyquist plots (P) displaying electrochemical impedance of as-synthesized 1T WS_2 nanosheets and as-grown 2H WS_2 nanostructures, including other reported MX_2 catalysts for comparison. Reproduced from Lukowski et al.[38] with permission of the Royal Society of Chemistry.

counterparts. Second, disordered 1T $MoSe_2$ nanosheets (Figure 5H) were obtained by the hydrothermal method by tuning the amount of $NaBH_4$ for HER catalysis.[50] The intrinsic activity and abundant unsaturated defects as active sites led to a low overpotential (152 mV) at 10 mA cm^{-2} (Figure 5I), low Tafel slope of 52 mV/decade (Figure 5J), and insignificant electrochemical impedance of ~16 Ω (Figure 5K). Lukowski and co-workers reported that chemically exfoliated 1T WS_2 nanostructures transformed from 2H phase (Figures 5L and 5M) exhibited lower energy consumption at the same current density, fast electrode kinetics, and excellent electron transfer ability for HER (Figures 5N, 5O, and 5P).[38] Similarly, other metallic-group VIB TMDCs produced via liquid exfoliation and their improved HER electrocatalytic activity were also compared systematically with other phases.[29,67] These results emphasize that the phase of TMDCs plays a vitally important role in HER. It is promising to broaden the family of TMDC nanomaterials with the aim of developing high-performance and low-cost HER catalysts.

Innovative Design for Optimizing HER Activity

Even though the excellent performance by metallic TMDC nanomaterials for HER electrocatalysis has been established, disparity with the activity of Pt-based materials still remains. Therefore, researchers need to perform further studies to improve the HER catalytic activity of metallic TMDCs to a higher level. Here, we summarize four main aspects for enhancing HER catalytic performance: (1) promoting the intrinsic activity of catalytic active sites, (2) increasing the density of catalytic active sites, (3) improving the electrical conductivity of the electrode, and (4) strengthening mass transfer. For metallic TMDC nanomaterials, remarkable intrinsic activity has been verified earlier, and thus activity enhancement via the other three aspects can be achieved by innovative structural and compositional design.

Structural Design. Based on metallic TMDC nanomaterials, the ability to creatively design architectures affords a promising opportunity to enhance the HER performance of electrocatalysts. Wang and co-workers utilized the electrochemical intercalation of Li^+ ions (Figure 6A) to realize the formation of vertically standing 1T MoS_2 nanofilms (Figure 6B) grown on mirror polished glassy carbon (MPGC).[68] The 1T MoS_2 nanofilms by Li electrochemical intercalation to 1.1 V exhibit an onset potential of only 113 mV (Figure 6C) and small Tafel slope of 44 mV/decade. Such outstanding catalytic activity is due to the exposure of more active edges, the conductive scaffold, and the metallic nature. This intriguing and effective architecture design prefers to fulfill the phase transition of TMDCs and proliferate the density of active sites to optimize the electrocatalytic activity. To improve the electrical conductivity, phase-engineered low-resistance contacts of 1T MoS_2 on a monolayer 2H MoS_2 basal plane contributes to higher efficiency of charge injection, which can be measured on a single nanosheet exposed to the basal plane (Figure 6D).[69] The polarization curves for various contact resistances show that HER performance

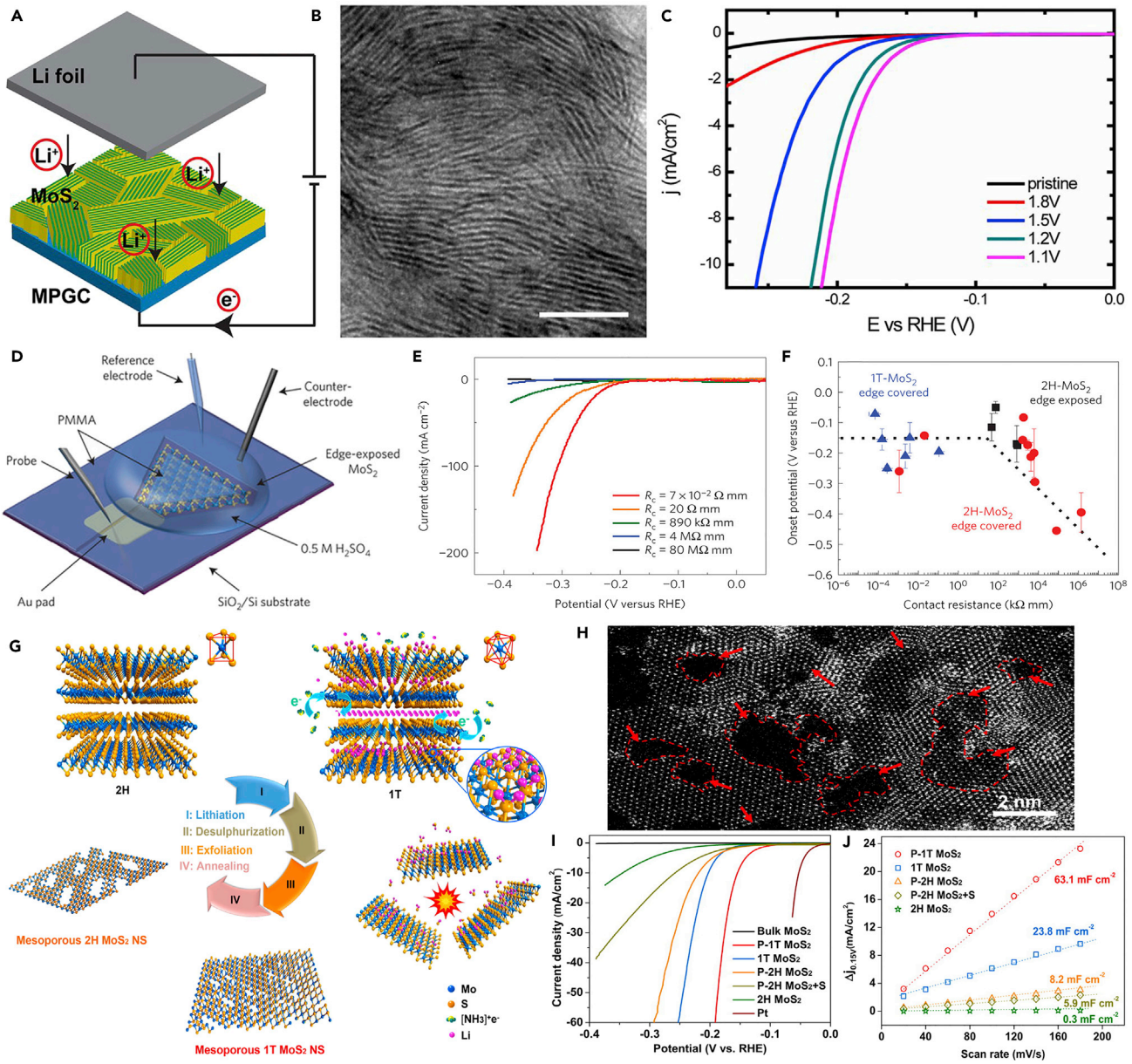

Figure 6. Structural Design for Optimizing HER Activity

(A–C) Schematic illustration of electrochemical lithiation for vertically aligned MoS_2 nanofilms (A), TEM image of MoS_2 by Li electrochemical intercalation to 1.1 V versus Li^+/Li (scale bar, 10 nm) (B), and polarization curves of pristine and lithiated MoS_2 on MPGC (C). Reprinted from Wang et al.[68]

(D–F) Schematic representation of the configuration showing a single layer of MoS_2 deposited on SiO_2 and contacted by a gold pad electrode (D). The counter and reference electrodes are glassy carbon and Ag/AgCl electrode, respectively. The entire substrate is covered with poly(methylmethacrylate) (PMMA), with the exception of a window on top of the edges of the MoS_2 nanosheet. Only the catalyst contacts with the electrolyte (0.5 M H_2SO_4). (E) Polarization curves measured on as-prepared MoS_2 with various contact resistances from 80 MΩ mm down to 7×10^{-2} Ω mm. The activity increases rapidly with decreasing contact resistance. (F) The relationship between the contact resistance and HER onset potential on edge-covered 1T MoS_2, edge-covered 2H MoS_2, and edge-exposed 2H MoS_2. Reprinted by permission from Springer Customer Service Centre GmbH: Springer Nature, *Nature Materials* Voiry et al.,[69] copyright 2016.

(G–J) Schematic illustration of the synthetic method for porous 1T MoS_2 nanosheets (P-1T-MoS_2) from bulk counterparts (G), HRSTEM image of porous 1T MoS_2 nanosheets (in which the pores are marked by red dashed lines and arrows) (H), polarization curves after iR correction showing the catalytic performance of as-prepared MoS_2 catalysts (I), and the linear fit plots showing the double-layer capacitance for as-prepared MoS_2 samples, which represents the active surface area (J). Reprinted from Zhu et al.[71]

increases with a decrease in contact resistance, irrespective of whether the edges or basal plane are exposed (Figure 6E). Figure 6F demonstrates that the basal plane of 2H MoS_2, considered to be less catalytically active, possesses HER performance comparable to that of the corresponding 1T phase by improving the electrical coupling (or reducing the contact resistance) between the substrate and catalyst in a phase-patterned technique. It is believed that this novel structural design of large-area electrodes with low contact resistance may provide new insights into MoS_2 nanosheets for HER. Furthermore, porous nanostructures can create more catalytic active sites and improve the mass transfer and gas permeability effectively during electrolysis, attracting plenty of interest for the structural design of electrocatalysts.[61,70] A comprehensive understanding reported by Yin et al.[71] elucidated a unique and unambiguous study on catalytic behavior of mesoporous 1T MoS_2 during the HER process. This nanostructure is designed and manufactured by a liquid ammonia-assisted lithiation route (Figure 6G), including lithiation, desulfurization, and exfoliation. The obvious porous feature and typical 1T phase structure (Figure 6H) endow the catalyst with a high density of catalytic active sites, excellent mass transfer, and remarkable intrinsic activity. As a result, porous 1T MoS_2 nanosheets afford a current density of 10 mA cm^{-2} at only 153 mV of overpotential (Figure 6I). The highest value of double-layer capacitance (Figure 6J) further demonstrates the largest active surface area of porous 1T MoS_2 nanosheets among as-prepared samples. This study offers new opportunities to identify the critical factors that influence the catalytic activity of MoS_2, which paves the way to design new architectures of 2D layered materials for further promotion of electrocatalytic performance. In summary, structural design is an effective strategy to further strengthen the catalytic ability of metallic TMDC nanomaterials, and we emphasize it here to encourage more innovatively designed architectures to emerge to facilitate this field of research.

Compositional Design. Both theoretical calculations and experimental measurements have demonstrated that the composition of the catalysts has a significant influence on the inherent HER activity.[37,72,73] In this section, we mainly focus on the compositional design of metallic TMDC-based nanomaterials for HER performance enhancement, which is separated into two parts: hybrid nanostructures and single-crystalline catalysts. Previously, our group developed a porous hybrid nanostructure composed of amorphous Ni–Co complexes and 1T MoS_2 (PHNCMs) via a solvothermal strategy with hydrazine-induced phase transformation (Figure 7A) for water splitting.[61] The hybrid was successfully synthesized and high porosity formed simultaneously (Figure 7B). Compared with the single-component samples, PHNCMs need only 70 mV of overpotential to afford a current density of 10 mA cm^{-2} (Figure 7C) for HER, which suggests that the diversification of active components plays a pivotal role in boosting HER performance. This work provides novel insight into optimizing HER activity on the basis of metallic TMDCs by introducing other active amorphous components, increasing the porosity, and adding the stabilizer mentioned above. Moreover, the N-doped 1T-2H $MoSe_2$/graphene (N-$MoSe_2$/VG) shell/core nanoflake arrays were synthesized by Deng and co-workers as a highly competitive earth-abundant HER catalyst.[74] Through thermal ammonia treatment of 2H $MoSe_2$/VG nanoflake arrays (Figure 7D), 1T $MoSe_2$ and N doping was introduced into the pristine array structures and the morphology of arrays remained unchanged (Figures 7E and 7F). The advantages are as follows. First, hybridization of N-doped 1T-2H $MoSe_2$ with vertical graphene contributes to a large surface area, fast electron transfer, and modified mass transport. The high mechanical strength and structural stability of the graphene scaffold can also maintain the long-term polarization ability of the electrode. Therefore, superior HER performance

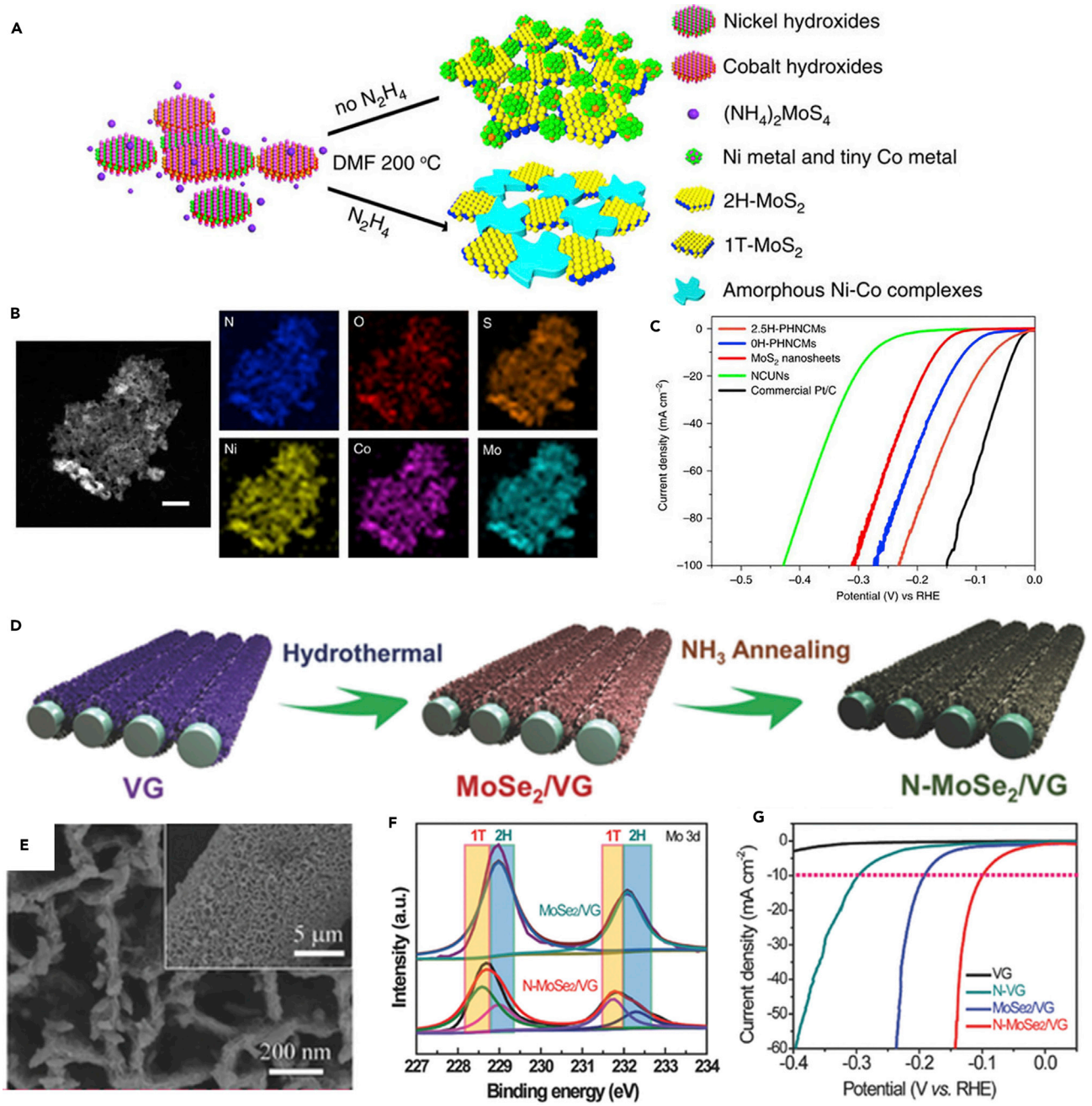

Figure 7. Compositional Design of the Hybrid Nanomaterials

(A–C) Schematic illustration of the formation of hybrid nanostructures composed of 1T MoS_2 and amorphous Ni-Co complexes via hydrazine-induced phase transformation (A); STEM image and energy-dispersive X-ray elemental mapping spectra of the as-prepared PHNCMs showing the porous feature and uniform element distribution of N (blue), O (red), S (orange), Ni (yellow), Co (pink), and Mo (cyan) (scale bar, 50 nm) (B); and polarization curves exhibiting electrocatalytic activities of the as-prepared PHNCMs and commercial Pt/C as a contrast for HER (the number before PHNCMs is the number of milliliters of hydrazine added to the reaction system) (C). Reprinted from Li et al.[61]

(D–G) Schematic illustration of the synthetic procedure (D) and SEM image (E) of N-$MoSe_2$/VG shell/core arrays. Inset in (E): SEM image of the corresponding sample for a large-scale view. (F) The XPS spectra of Mo 3d regions for N-$MoSe_2$/VG and $MoSe_2$/VG. (G) Polarization abilities for HER of the as-synthesized hybrid samples. Reprinted with permission from Deng et al.[74] Copyright 2017 Wiley-VCH Verlag GmbH & Co. KGaA.

can be obtained (45 mV of onset potential and 98 mV of overpotential at 10 mA cm^{-2}, as shown in Figure 8G). The combination of other active components or remarkable scaffolds is an effective method of optimizing the composition and is summarized here to provide inspiration for further studies. Although there is also some progress emerging in this field, we cover the characteristic advances for in-depth analyses and development possibilities.

For a more complete review of this rapidly growing field, single-crystalline catalysts have been developed for atomically precise investigation on crystal structural changes and the expansion of novel materials. 2D layered single-crystalline metallic $MoTe_2$ was synthesized by Seok et al.[75] for durable and effective HER electrocatalysis. The defect-free single-crystalline nature and typical 1T′ phase structure with multilayered monoclinic symmetry are verified by the XRD pattern (Figure 8A) and HRSTEM image (Figure 8B), which are beneficial to study the changes in lattice structure from the perspective of atomic precision. Compared with the 2H counterpart, 1T′ $MoTe_2$ exhibits higher intrinsic catalytic activity (Figure 8C). Hydrogen adsorption on as-prepared 1T′ $MoTe_2$ resulted in spontaneous Peierls-type lattice distortion (Figures 8D and 8E), activating the HER catalysis, which was supported by the XPS spectra (Figure 8F) with slight energy shifts of the wider peaks. Given this rigorous structural illustration for the HER process, this work provides profound insights into the influence of atomic lattice geometry on hydrogen evolution. For the development of novel and desirable catalysts with no contamination and high crystalline quality, Yuan and co-workers report a facile CVD method to synthesize metallic VS_2 singe-crystal nanosheets (Figures 8G and 8H) for a potential scale-up fabrication and practical HER catalysis.[76] The metallic characteristic (Figure 8I) contributes to the remarkable HER activity (Figure 8J) and fast reaction kinetics (Figure 8K) approaching that of Pt. Notably, this distinctive catalyst shows self-optimizing behavior during electrolysis (Figure 8K), which is a compelling feature for HER electrocatalysis and opens a new door to the use of metallic-group VB catalysts.[23] Metallic single-crystalline NbS_2 nanoflakes were synthesized via a facile CVD method to serve as an improved electrocatalyst for hydrogen generation.[77] Crystalline nature is considered as indispensable factor affecting Tafel slope, turnover frequency, and stability of the catalysts.[78] Thus, engineering the crystalline structure is indeed important for enhancing electrocatalytic activity.

Influences on HER Electrocatalysis

With the rapid development of this growing field, other influences have been investigated to further explore HER electrocatalysis over TMDCs and enhance the activity. It is important to focus on these comprehensive studies, which greatly expand our fundamental research and guide future directions not just for metallic TMDCs but also for all 2D layered TMDCs. First, stacking is a common phenomenon in 2D layered nanostructures and has a considerable effect on HER performance. An interlayer potential barrier has been proven in the process of electron transfer in the vertical direction in MoS_2 layers (Figure 9A).[79] This layer-dependent feature causes an inverse correlation between the number of layers and HER activity. Monolayer MoS_2 possesses the lowest overpotential (Figure 9B) and superior electrode kinetics (Figure 9C) except for Pt samples.[80] This result has inspired the ultrathin design for catalysts to increase the hopping efficiency of electrons in the vertical direction of stacking layers leading to high catalytic activity. Second, transition-metal doping has been widely utilized to systematically tune the structure and activity of TMDCs; this determines the hydrogen binding behavior onto the active sites. Tsai et al.[72] have reported that, according to computational results, the hydrogen adsorption free energies of 14 transition-metal dopants (Pt, Ni, Ru, Rh, Co, Fe, Mn, Ta, V, Nb,

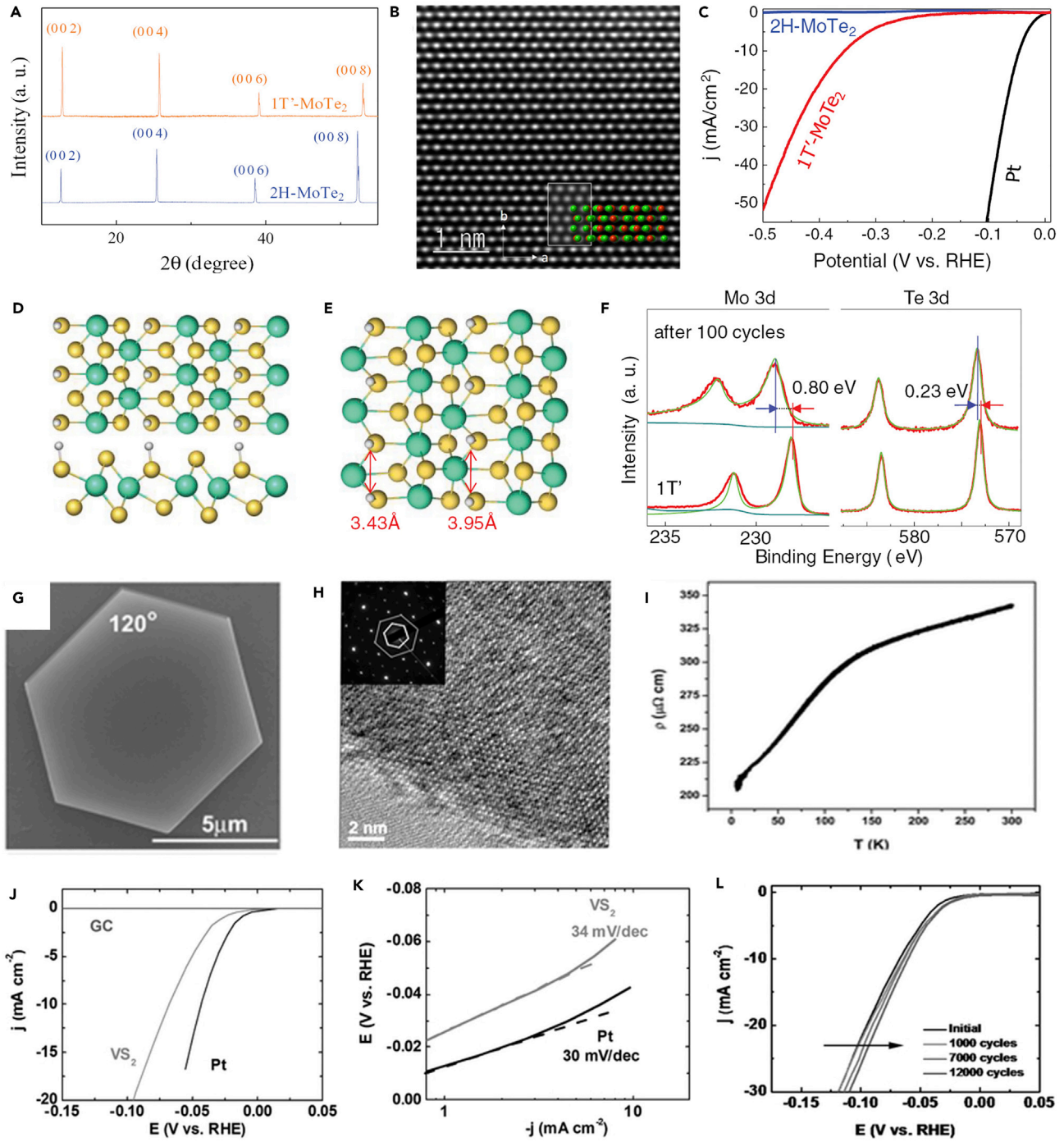

Figure 8. Single-Crystalline HER Catalysts

(A–F) XRD patterns of 2H and 1T′ $MoTe_2$ single crystals (A); HRSTEM image of 1T′ $MoTe_2$ observed along the (103) lattice planes (B); polarization curves of 2H $MoTe_2$ (blue), 1T′ $MoTe_2$ (red), and Pt (black) for HER (C); schematic lattice structure of 1T′ $MoTe_2$ with fully covered hydrogen atoms at α sites (D); Peierls-type distorted lattice structure of 1T″ $MoTe_2$ (E) spontaneously produced by the hydrogen adsorption in (D); and XPS comparisons of 1T′ $MoTe_2$ in Mo 3d and Te 3d regions before and after HER (F). Reprinted from Seok et al.[75]

(G–L) SEM image of a VS_2 nanosheet with dominant hexagonal shape for a single crystal (G), HRTEM image of a single-crystalline VS_2 nanosheet (inset shows the corresponding electron diffraction pattern; the well-defined hexagonal pattern and only one set of spots confirm the single-crystalline nature) (H), the relationship of resistivity with temperature (the resistivity of VS_2 increases as the temperature increases, which demonstrates the metallic behavior) (I), and polarization curves with iR correction (J), Tafel plots (K), and polarization curves (L) for single-crystalline VS_2 nanosheets after various cycles. Reprinted with permission from Yuan et al.[76] Copyright 2017 Wiley-VCH Verlag GmbH & Co. KGaA.

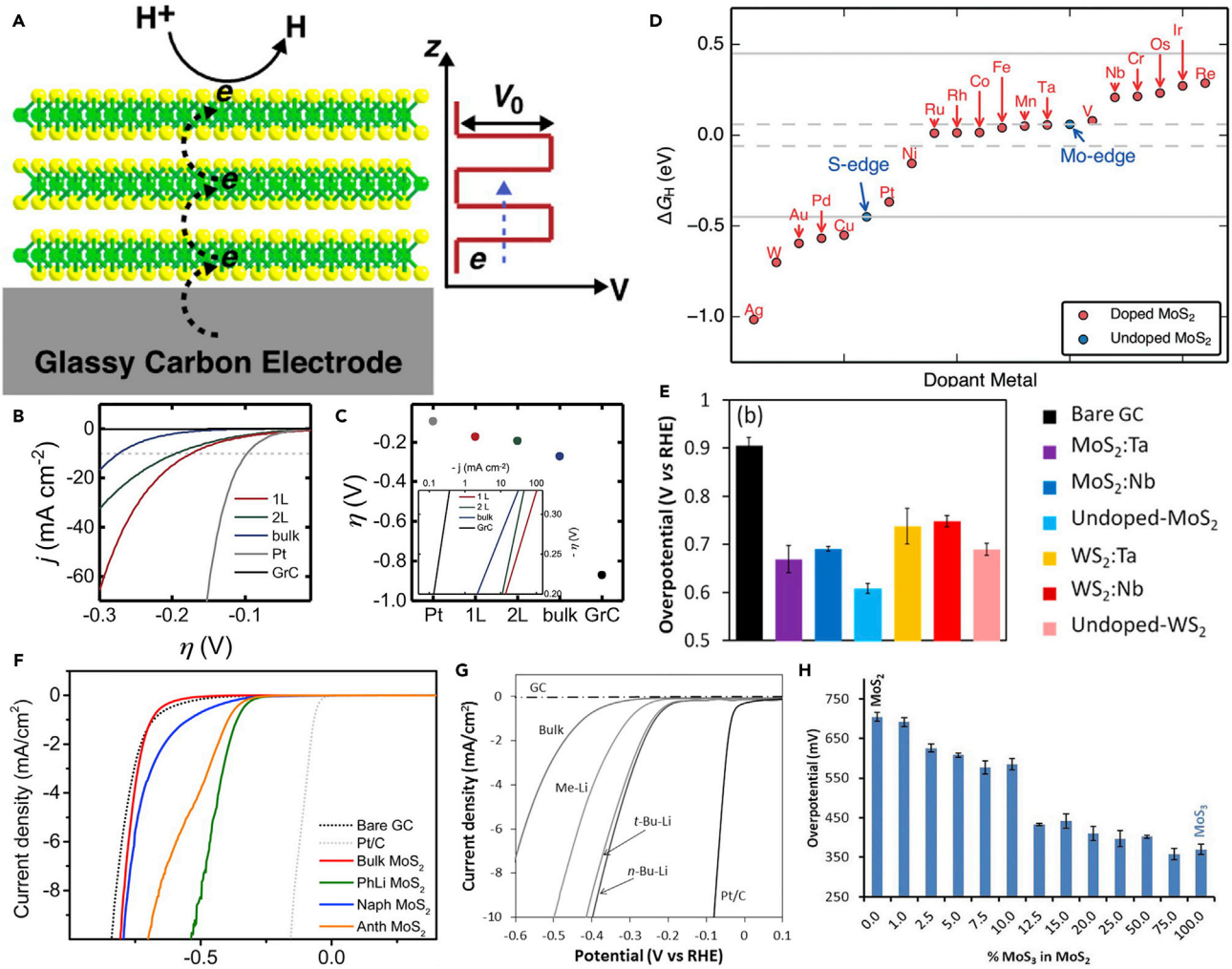

Figure 9. Influence Investigation on HER Electrocatalysis

(A) Schematic illustration of electron transfer in the vertically stacked MoS_2 layers. The potential distribution in the multilayer film and the potential barrier in the interlayer gap during electron transfer are shown on the right. Reprinted with permission from Yu et al.[79] Copyright 2014 American Chemical Society.

(B and C) Polarization curves of bare graphenic carbon (GrC), bulk, 2L, and 1L MoS_2 flakes for HER (B) and summary of overpotentials at the current density of 10 mA cm^{-2} for 1L, 2L, and bulk MoS_2 flakes, Pt, and GrC (C). The inset shows the corresponding Tafel slopes: GrC 273 mV/decade, bulk 114 mV/decade, 2L 210 mV/decade, and 1L 149 mV/decade. Reprinted from Parzinger et al.[80]

(D) Summary of ΔG_H of transition-metal-doped MoS_2. Reproduced from Tsai et al.[72] with permission of the Royal Society of Chemistry.

(E) Bar chart for a comparison of the overpotential of Nb-, Ta-doped, and undoped MoS_2 at 10 mA cm^{-2} for HER. Error bars correspond to standard deviations on the basis of triplicate measurements. Reprinted with permission from Chua et al.[82] Copyright 2016 American Chemical Society.

(F) HER polarization curves of MoS_2 untreated and after treatment with phenyllithium, naphthalenide, or anthracenide followed by exfoliation. Reprinted with permission from Tan et al.[83] Copyright 2016 American Chemical Society.

(G) Polarization curves of as-prepared bulk MoS_2 and counterparts after exfoliation with methyllithium, *n*-butyllithium, and *tert*-butyllithium for HER. Reprinted with permission from Ambrosi et al.[84] Copyright 2015 Wiley-VCH Verlag GmbH & Co. KGaA.

(H) Bar chart for comparison of the overpotentials at 10 mA cm^{-2} of MoS_2 with different amounts of MoS_3 impurities. Reproduced from Latiff et al.[85] with permission of the Royal Society of Chemistry.

Cr, Os, Ir, and Re) approach the thermoneutral values of undoped S-edge in MoS_2, especially for Ru, Rh, Co, Fe, Mn, and Ta, which are even lower than that of the already active undoped Mo-edge in MoS_2 (Figure 9D). This concept of tunable hydrogen binding provides accessible design for TMDCs catalysts with numerous choices for synthesis. Previous studies of V-doped MoS_2 nanosheets demonstrated improved HER performance, offering a novel strategy to regulate intrinsic electrical

properties for electrocatalysis via doping.[81] However, dopants may have a negative effect on HER catalysis in practical experimental measurements. The p-type Nb- and Ta-doped MoS_2 and WS_2 were demonstrated to exhibit lower HER activity than the undoped counterparts (Figure 9E).[82] Therefore, it is necessary to choose dopants to facilitate HER catalysis on the basis of integration of theoretical and experimental investigations. Third, various organic ligands enable intercalation of TMDCs to realize 2H to 1T phase transition. Tan and co-workers have discovered the implications of aromatic-exfoliated TMDCs as catalysts for HER.[83] Figure 9F shows that PhLi MoS_2 performs best for HER polarization among as-prepared MoS_2 samples as a result of the increased edge sites and enhanced exposure of metal ion species. For alkane chain ligands, butyl is a better choice to promote exfoliation efficiency, resulting in a decrease in lateral size and number of layers.[84] The larger active surface area and available edge planes guarantee superior catalytic activity (Figure 9G). Hence, meticulous care is essential when selecting the intercalant for the expected utilizations. Furthermore, Mo- and W-based valence and oxide impurities inevitably appear in the TMDC products, which results in a highly catalytic effect toward the HER.[85] Compared with the corresponding oxide impurities, increasing overpotentials, and slowing down electrode kinetics, sulfide impurities have an interesting positive influence on HER activity. From the wide range of concentrations measured (Figures 9H), 12.5% MoS_3 was identified as the optimal proportion in MoS_2; additional impurities for decreasing the overpotential becomes less important beyond that concentration. In practical fundamental research, impurities are usually regarded as synthetic by-products and preferentially removed in the final products. This finding can serve as a creative platform to further optimize HER catalytic activity of electrode materials. Recently, biaxial tensile strain[86] and low hydrogen coverage[87] have been proposed to tune the hydrogen adsorption free energy on the surface of metallic NbS_2 catalysts for enhancement of catalytic activity. The above influences can act as a guideline for the future development of metallic TMDC electrocatalysts, which provide plenty of innovative routes to facilitate the process of HER catalysis.

Metallic TMDCs for Solar-Driven Hydrogen Production

In addition to electrochemical HER, solar-driven water splitting is also one of the most promising alternatives to realize high-efficiency hydrogen generation, converting solar energy to chemical fuel.[5,6] It is essential to carry out the conversion in a photovoltaics-electrolyzer system or an integrated photoelectrochemical (PEC) configuration, which enables and facilitates light harvesting and direct solar-to-fuel production.[88–90] In this process, a light absorber and a co-catalyst are indispensable. The former can produce electron-hole pairs upon illumination and the latter contributes to charge transfer and achieves fuel production. It has been reported that one single semiconductor, such as TiO_2,[91] CdS,[92] and ZnS,[93] as photocatalyst can help to catalyze water splitting under visible light with suitable band gap. However, rapid recombination of photogenerated electrons and holes in these semiconductors is a significant challenge in the development of photocatalytic HER.[94] Therefore, the introduction of a co-catalyst is an effective way to address this problem. An excellent co-catalyst can also provide more catalytic active sites to reduce the activation energy of the water-splitting reaction.[95] Although Pt-based materials exhibit good activity, the earth-abundant catalysts are still attracting great attention because of the high cost of catalysts containing noble metals. Here, we discuss photovoltaics-electrolyzer and PEC systems based on hybrids of metallic MoS_2 and other semiconductors. Outstanding performances are expected to create momentum in pursuing highly active and robust photocatalysts.

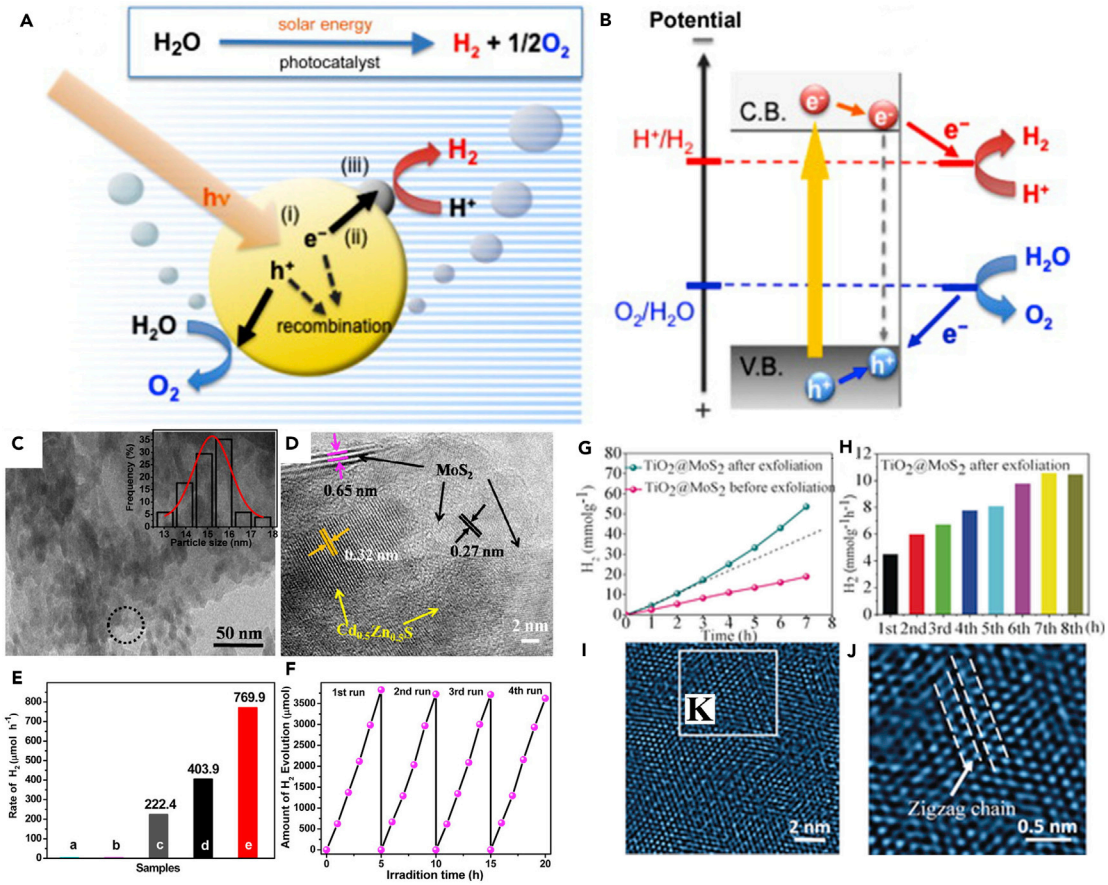

Figure 10. Photochemical Hydrogen Generation over Hybrids of 1T MoS_2 and a Light Absorber

(A and B) Schematic illustration (A) and fundamental principle (B) of photocatalytic water splitting reactions. Reprinted from Abe et al.[88]

(C–F) TEM (C) and HRTEM (D) images of the as-prepared 1T Li_xMoS_2 (1.0 wt %)/$Cd_{0.5}Zn_{0.5}S$ nanostructures (inset in C shows the corresponding size distribution of the particles), photocatalytic H_2 production rates of as-prepared (a) MoS_2, (b) Li_xMoS_2, (c) $Cd_{0.5}Zn_{0.5}S$, (d) 2H MoS_2 (1.0 wt %)/$Cd_{0.5}Zn_{0.5}S$, and (e) 1T Li_xMoS_2 (1.0 wt %)/$Cd_{0.5}Zn_{0.5}S$ (E), and time cycle of photocatalytic H_2 production over 1T Li_xMoS_2 (1.0 wt %)/$Cd_{0.5}Zn_{0.5}S$ (F). Reprinted with permission from Du et al.[96] Copyright 2016 American Chemical Society.

(G–K) H_2 accumulation (G) and production rate (H) over as-exfoliated TiO_2@MoS_2 at each hour, HRTEM image of MoS_2 in the as-exfoliated sample after 7 hr photocatalytic measurement (I), and HRTEM image (J) for a large view of the marked region in (K). The arrows points to the zigzag chains in the 1T′ structure. Reprinted with permission from Wang et al.[98] Copyright 2016 Wiley-VCH Verlag GmbH & Co. KGaA.

Photochemical Water Splitting for Hydrogen Generation

The procedure for photochemical water splitting for generating H_2 and O_2 on a heterogeneous catalyst is shown in Figure 10A. First, photons are absorbed by the semiconductor with higher energies than the band gap, forming electron (e^-)-hole (h^+) pairs. Second, electron and hole separate from each other. Third, the water-splitting reaction takes place between carriers and reactants on the surface of the catalyst.[88] However, electron and hole may also tend to recombine with each other and thus a co-catalyst needs to be introduced into the system. The fundamental requirements should be met by the photocatalyst whereby the bottom of the conduction band must be more negative than the reduction potential of H^+/H_2, and the top of the valence band must be more positive than the oxidation potential of H_2O/O_2 (Figure 10B). According to this standard, a few efficient and earth-abundant photocatalysts have been fabricated. $Cd_{0.5}Zn_{0.5}S$ nanoparticles loaded on metallic 1T Li_xMoS_2 has been studied for enhancing photocatalytic hydrogen production.[96] 1T Li_xMoS_2 (1 wt %)/$Cd_{0.5}Zn_{0.5}S$ hybrid nanostructures (Figures 10C and 10D) show better photocatalytic performance in H_2 generation rate than other samples (Figure 10E). The

remarkable durability and recycling performance of the hybrid is shown in Figure 10F. It turns out that 1T MoS_2 is an efficient co-catalyst as an alternative for precious metals in H_2 generation, as a result of high conductivity, proliferative active sites on both edges and the basal planes, and protective effects on electron-hole recombination. Similarly, other fascinating hybrid photocatalysts, such as 1T MoS_2/CdS,[28] 1T WS_2/TiO_2,[48] and 1T MoS_2/TiO_2,[97] that demonstrate the great potential of metallic TMDCs as co-catalysts in photocatalysis to replace noble-metal materials have been also developed.

To clarify the changes in 1T MoS_2 during photocatalysis, Wang et al.[98] prepared a hybrid of TiO_2@1T MoS_2 via hydrothermal exfoliation to investigate HER photocatalytic activities as a function of phase evolution. As shown in Figure 10G, the amount of H_2 over TiO_2@MoS_2 after exfoliation increased linearly along with the reaction time in comparison with the straight line of TiO_2@MoS_2 before exfoliation. The photocatalytic activity of TiO_2@MoS_2 after exfoliation increased gradually and optimization was completed after 7 hr (Figure 10H). During the HER process, the 1T phase gradually relaxed into a highly distorted 1T′ structure. The distorted 1T′ phase with the zigzag chains of superlattice structures with Mo clusters can be observed in Figures 10I and 10J, which corresponds to truly active phase and catalytic sites. The self-optimization of the photocatalyst provides a new path to enhance catalytic activity in the photochemical environment.

PEC Hydrogen Generation from Water Splitting

Figures 11A–11C present the configurations of the PEC system. In comparison with photochemical HER, the reaction mechanism of PEC HER is a little different. For an n-type semiconductor photoanode, first, electron-hole pairs are generated on the anode with higher energies than the band gap under light irradiation, at which time O_2 is produced by reaction between water and holes. Second, photogenerated electrons transfer to the cathode. Then H^+ is reduced to produce H_2 by photogenerated electrons. In this system, an external voltage is attached as a power supply to overcome overpotential and other energy losses.[88,94] In the case of a p-type semiconductor photocathode, H_2 evolves on this semiconductor surface, whereas water is oxidized on the counter electrode. A tandem system contains a p-type semiconductor electrode as cathode and an n-type semiconductor electrode as anode without an external bias. To investigate the HER catalytic performance of metallic TMDCs in the PEC system, they usually hybridize with a p-type semiconductor as photocathode, measured in a typical three-electrode system for HER performance. Ding et al.[99] have shown that an integrated heterostructure (Figures 11D and 11E) of chemically exfoliated 1T MoS_2 and planar p-type silicon (p-Si) is an efficient and robust photocathode for PEC HER. After equilibrium, the 1T MoS_2/Si heterostructure shows a negative signal, which is similar to downward band bending of p-Si and is consistent with the band position and band alignment between p-Si and 1T MoS_2 (Figures 11F and 11G). As shown in Figure 11H, the onset potential is +0.25 V versus a reversible hydrogen electrode (RHE) and the current density at 0 V versus RHE reaches 17.6 mA cm^{-2} for an as-prepared 1T MoS_2/Si heterostructure. The introduction of 1T MoS_2 as co-catalyst also leads to slow carrier recombination dynamics and efficient charge carrier separation. Moreover, low charge-transfer resistance and long-term stability make it a promising replacement for noble-metal photocathodes for PEC HER catalysis.

CONCLUSIONS AND PERSPECTIVES

The utilization of metallic TMDCs for widespread energy conversion applications has emerged to facilitate the study of high-efficiency and earth-abundant catalysts and

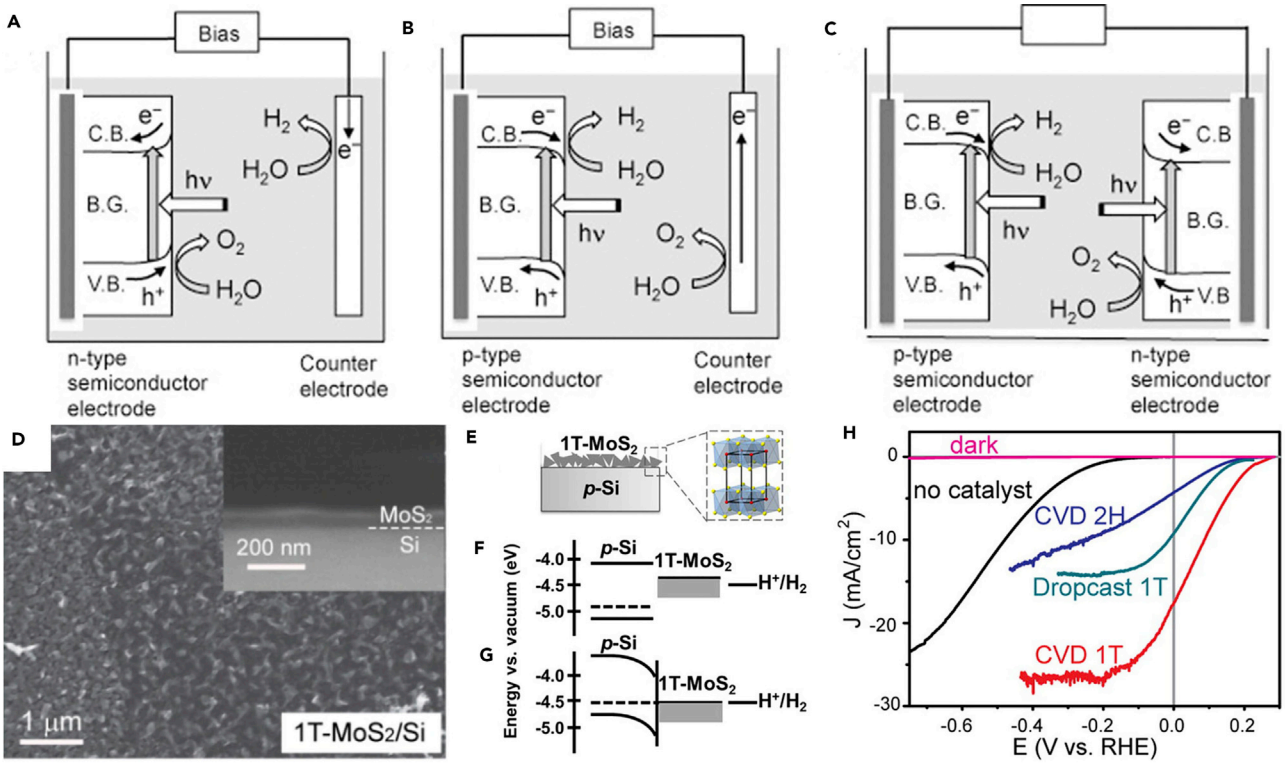

Figure 11. PEC Configurations and Hydrogen Production Based on a 1T MoS_2 Electrode

(A–C) PEC configurations using an n-type semiconductor photoanode (A), a p-type semiconductor photocathode (B), and tandem system (C). Reprinted from Abe et al.[88]

(D–H) SEM images of 1T MoS_2/Si heterostructures for top-down and cross-sectional (inset) views (D); schematic illustration of 1T MoS_2 supported on p-Si (E); schematic band energy diagram of p-Si, 1T MoS_2, and H^+/H_2 redox couple at 0 V versus RHE in the dark before (F) and after (G) equilibrium; and polarization curves of as-prepared and drop-casted samples and a bare Si electrode as a comparison measured in 0.5 M H_2SO_4 under simulated 1 sun irradiation (H). Reprinted with permission from Ding et al.[99] Copyright 2014 American Chemical Society.

innovative nanotechnologies. For fundamental research, the characteristics of the structural features and diversified synthetic strategies of this category of materials have been intensively established to accurately control structures and tune the properties of target products and have shown considerable success. Many metallic TMDCs and their composites play a vital role in electrochemical and solar-driven HER catalysis. On the basis of the two core advantages, that is, proliferative catalytic active sites and fast electrode kinetics and charge transport, metallic TMDCs exhibit outstanding catalytic performance compared with that of their semiconducting counterparts and a large number of other non-noble-metal catalysts, which will encourage researchers to further optimize the catalysts for better performance and acquire a comprehensive understanding of the mechanism underlying these achievements. We also highlight the state-of-the-art innovations for improving the efficiency of energy conversion. These recently reported breakthroughs are essential to fundamental research and practical applications.

In this review, we have summarized the recent progress in metallic TMDC nanomaterials and their composites in terms of distinctive characteristics, synthetic methodologies, and electrochemical and solar-driven HER catalytic applications. Several advances have been realized in this promising domain. However, some challenges still need to be addressed, which will help to provide more tangible guidelines for the future of this field.

Large-Scale Fabrication

The current synthetic strategies can be only applied to fundamental research in the laboratory. More efforts should be devoted to large-scale preparation for industrial and social deployment. With a comprehensive understanding, solvothermal methods and vapor-phase strategies are appropriate for completing this goal. For solvothermal methods, it is significant to achieve success in the transition of the reaction conditions from fundamental research to practical large-scale synthesis. Modified reaction parameters are usually available for large-scale fabrication. The repeatability and surface treatment of massive products are also nonnegligible factors that must be realized in the industrialization of these earth-abundant materials. For vapor-phase strategies, high manufacturing cost is the most important issue to be addressed. The cost can be controlled with regard to precursors, instruments, and substrates in future development. For both synthetic routes, the instability issue of the final products alos needs to be resolved because metallic TMDCs have high ground-state energies, especially group VIB TMDCs. Therefore, more strategies should be created from the point of view of structure and scaffold to produce and stabilize high-quality and uniform metallic TMDCs for practical use.

Mechanistic Study

From the perspective of integrated development of this field, it is not enough that only new catalysts emerge. In-depth advanced mechanistic understanding of catalytic reactions over metallic TMDCs at atomic or molecular level must be explored simultaneously. Catalyst behavior during reactions and at the surface/interface can be characterized and monitored in real time via *in operando* characterization technologies, such as *in situ* HRTEM, EXAFS, and so on. There are numerous fundamental issues outstanding at present, such as the reaction behavior of authentic active atoms, interface characteristics, and the precise capture of reaction intermedia. Through investigation of the overall reaction mechanism, accurate regulation and control of HER catalysis, as well as optimization of the catalytic performance of the electrode materials, are desirable.

Feasibility of Catalysts

There are many apparent differences between practical application and fundamental research. The as-prepared catalysts should be assessed for feasibility in practical industrial wholesale catalysis. For instance, excellent durability is one of the most significant benchmarks for feasibility of catalysts. In contrast to pristine catalytic activity maintained several hours in fundamental research, catalysts in practical large-scale catalysis need to maintain high catalytic ability for a longer time by orders of magnitude. Thus, remarkable design of catalysts and indispensable scaffolds may be at the forefront of development. It is reasonable to believe that we will have a full understanding of metallic TMDC nanomaterials from all perspectives to fulfill the demands of practical HER catalysis in the future.

ACKNOWLEDGMENTS

X.W. and H.L. acknowledge financial support from the National Natural Science Foundation of China (21431003, 21521091, and 11605201), the China Ministry of Science and Technology (contract no. 2016YFA0202801), and the State Key Project of Fundamental Research for Nanoscience and Nanotechnology (2014CB848900).

AUTHOR CONTRIBUTIONS

X.W. supervised the preparation of this review article. X.W. and H.L. conceived the topic. H.L. contributed to most of the writing, and X.J. and Q.Z. contributed to some

content and figures. X.W. and H.L. revised and finalized the manuscript. All authors approved the final version of the manuscript.

REFERENCES AND NOTES

1. Chu, S., and Majumdar, A. (2012). Opportunities and challenges for a sustainable energy future. Nature *488*, 294–303.
2. Schlapbach, L., and Züttel, A. (2001). Hydrogen-storage materials for mobile applications. Nature *414*, 353–358.
3. Steele, B.C.H. (1999). Fuel-cell technology: running on natural gas. Nature *400*, 619–621.
4. Lewis, N.S., and Nocera, D.G. (2006). Powering the planet: chemical challenges in solar energy utilization. Proc. Natl. Acad. Sci. USA *103*, 15729–15735.
5. Maeda, K., Teramura, K., Lu, D., Takata, T., Saito, N., Inoue, Y., and Domen, K. (2006). Photocatalyst releasing hydrogen from water. Nature *440*, 295.
6. Mallouk, T.E. (2013). Water electrolysis: divide and conquer. Nat. Chem. *5*, 362–363.
7. Jiao, Y., Zheng, Y., Jaroniec, M., and Qiao, S.Z. (2015). Design of electrocatalysts for oxygen- and hydrogen-involving energy conversion reactions. Chem. Soc. Rev. *44*, 2060–2086.
8. Yin, H., Zhao, S., Zhao, K., Muqsit, A., Tang, H., Chang, L., Zhao, H., Gao, Y., and Tang, Z. (2015). Ultrathin platinum nanowires grown on single-layered nickel hydroxide with high hydrogen evolution activity. Nat. Commun. *6*, 6430.
9. Jin, Y., Wang, H., Li, J., Yue, X., Han, Y., Shen, P.K., and Cui, Y. (2016). Porous MoO_2 nanosheets as non-noble bifunctional electrocatalysts for overall water splitting. Adv. Mater. *28*, 3785–3790.
10. Lu, Z., Zhu, W., Yu, X., Zhang, H., Li, Y., Sun, X., Wang, X., Wang, H., Wang, J., and Luo, J. (2014). Ultrahigh hydrogen evolution performance of under-water "superaerophobic" MoS_2 nanostructured electrodes. Adv. Mater. *26*, 2683–2687.
11. Chen, W.F., Sasaki, K., Ma, C., Frenkel, A.I., Marinkovic, N., Muckerman, J.T., Zhu, Y., and Adzic, R.R. (2012). Hydrogen-evolution catalysts based on non-noble metal nickel-molybdenum nitride nanosheets. Angew. Chem. Int. Ed. *51*, 6131–6135.
12. Zhang, G., Wang, G., Liu, Y., Liu, H., Qu, J., and Li, J. (2016). Highly active and stable catalysts of phytic acid-derivative transition metal phosphides for full water splitting. J. Am. Chem. Soc. *138*, 14686–14693.
13. Liao, L., Wang, S., Xiao, J., Bian, X., Zhang, Y., Scanlon, M.D., Hu, X., Tang, Y., Liu, B., and Girault, H.H. (2014). A nanoporous molybdenum carbide nanowire as an electrocatalyst for hydrogen evolution reaction. Energy Environ. Sci. *7*, 387–392.
14. Li, H., Chen, S., Lin, H., Xu, X., Yang, H., Song, L., and Wang, X. (2017). Nickel diselenide ultrathin nanowires decorated with amorphous nickel oxide nanoparticles for enhanced water splitting electrocatalysis. Small *13*, 1701487.
15. Chia, X., Eng, A.Y.S., Ambrosi, A., Tan, S.M., and Pumera, M. (2015). Electrochemistry of nanostructured layered transition-metal dichalcogenides. Chem. Rev. *115*, 11941–11966.
16. He, Z., and Que, W. (2016). Molybdenum disulfide nanomaterials: structures, properties, synthesis and recent progress on hydrogen evolution reaction. Appl. Mater. Today *3*, 23–56.
17. Yang, H., Kim, S.W., Chhowalla, M., and Lee, Y.H. (2017). Structural and quantum-state phase transitions in van der Waals layered materials. Nat. Phys. *13*, 931.
18. Xu, M., Liang, T., Shi, M., and Chen, H. (2013). Graphene-like two-dimensional materials. Chem. Rev. *113*, 3766–3798.
19. Sun, Y., Gao, S., and Xie, Y. (2014). Atomically-thick two-dimensional crystals: electronic structure regulation and energy device construction. Chem. Soc. Rev. *43*, 530–546.
20. Chhowalla, M., Shin, H.S., Eda, G., Li, L.-J., Loh, K.P., and Zhang, H. (2013). The chemistry of two-dimensional layered transition metal dichalcogenide nanosheets. Nat. Chem. *5*, 263–275.
21. Voiry, D., Mohite, A., and Chhowalla, M. (2015). Phase engineering of transition metal dichalcogenides. Chem. Soc. Rev. *44*, 2702–2712.
22. Voiry, D., Yang, J., and Chhowalla, M. (2016). Recent strategies for improving the catalytic activity of 2D TMD nanosheets toward the hydrogen evolution reaction. Adv. Mater. *28*, 6197–6206.
23. Liu, Y., Wu, J., Hackenberg, K.P., Zhang, J., Wang, Y.M., Yang, Y., Keyshar, K., Gu, J., Ogitsu, T., and Vajtai, R. (2017). Self-optimizing, highly surface-active layered metal dichalcogenide catalysts for hydrogen evolution. Nat. Energy *2*, 17127.
24. Wang, Q.H., Kalantar-Zadeh, K., Kis, A., Coleman, J.N., and Strano, M.S. (2012). Electronics and optoelectronics of two-dimensional transition metal dichalcogenides. Nat. Nanotechnol. *7*, 699–712.
25. Kappera, R., Voiry, D., Yalcin, S.E., Branch, B., Gupta, G., Mohite, A.D., and Chhowalla, M. (2014). Phase-engineered low-resistance contacts for ultrathin MoS_2 transistors. Nat. Mater. *13*, 1128–1134.
26. Eda, G., Yamaguchi, H., Voiry, D., Fujita, T., Chen, M., and Chhowalla, M. (2011). Photoluminescence from chemically exfoliated MoS_2. Nano Lett. *11*, 5111–5116.
27. Voiry, D., Salehi, M., Silva, R., Fujita, T., Chen, M., Asefa, T., Shenoy, V.B., Eda, G., and Chhowalla, M. (2013). Conducting MoS_2 nanosheets as catalysts for hydrogen evolution reaction. Nano Lett. *13*, 6222–6227.
28. Liu, Q., Li, X., He, Q., Khalil, A., Liu, D., Xiang, T., Wu, X., and Song, L. (2015). Gram-Scale Aqueous Synthesis of stable few-layered 1T-MoS_2: applications for visible-light-driven photocatalytic hydrogen evolution. Small *11*, 5556–5564.
29. Lukowski, M.A., Daniel, A.S., Meng, F., Forticaux, A., Li, L., and Jin, S. (2013). Enhanced hydrogen evolution catalysis from chemically exfoliated metallic MoS_2 nanosheets. J. Am. Chem. Soc. *135*, 10274–10277.
30. Liu, L., Kumar, S.B., Ouyang, Y., and Guo, J. (2011). Performance limits of monolayer transition metal dichalcogenide transistors. IEEE Trans. Electron. Devices *58*, 3042–3047.
31. Ding, Y., Wang, Y., Ni, J., Shi, L., Shi, S., and Tang, W. (2011). First principles study of structural, vibrational and electronic properties of graphene-like MX_2 (M = Mo, Nb, W, Ta; X = S, Se, Te) monolayers. Physica B Condens. Matter *406*, 2254–2260.
32. Heising, J., and Kanatzidis, M.G. (1999). Structure of restacked MoS_2 and WS_2 elucidated by electron crystallography. J. Am. Chem. Soc. *121*, 638–643.
33. Eda, G., Fujita, T., Yamaguchi, H., Voiry, D., Chen, M., and Chhowalla, M. (2012). Coherent atomic and electronic heterostructures of single-layer MoS_2. ACS Nano *6*, 7311–7317.
34. Papageorgopoulos, C.A., and Jaegermann, W. (1995). Li intercalation across and along the van der Waals surfaces of MoS_2 (0001). Surf. Sci. *338*, 83–93.
35. Sandoval, S.J., Yang, D., Frindt, R.F., and Irwin, J.C. (1991). Raman study and lattice dynamics of single molecular layers of MoS_2. Phys. Rev. B *44*, 3955.
36. Putungan, D.B., Lin, S.H., and Kuo, J.L. (2015). A first-principles examination of conducting monolayer 1T′-MX_2 (M = Mo, W; X = S, Se, Te): promising catalysts for hydrogen evolution reaction and its enhancement by strain. Phys. Chem. Chem. Phys. *17*, 21702–21708.
37. Tsai, C., Chan, K., Nørskov, J.K., and Abild-Pedersen, F. (2015). Theoretical insights into the hydrogen evolution activity of layered transition metal dichalcogenides. Surf. Sci. *640*, 133–140.
38. Lukowski, M.A., Daniel, A.S., English, C.R., Meng, F., Forticaux, A., Hamers, R.J., and Jin, S. (2014). Highly active hydrogen evolution catalysis from metallic WS_2 nanosheets. Energy Environ. Sci. *7*, 2608–2613.
39. Voiry, D., Yamaguchi, H., Li, J., Silva, R., Alves, D.C.B., Fujita, T., Chen, M., Asefa, T., Shenoy, V.B., and Eda, G. (2013). Enhanced catalytic activity in strained chemically exfoliated WS_2 nanosheets for hydrogen evolution. Nat. Mater. *12*, 850–855.
40. Niu, L., Coleman, J.N., Zhang, H., Shin, H., Chhowalla, M., and Zheng, Z. (2016). Production of Two-dimensional nanomaterials via liquid-based direct exfoliation. Small *12*, 272–293.

41. Ganal, P., Olberding, W., Butz, T., and Ouvrard, G. (1993). Soft chemistry induced host metal coordination change from octahedral to trigonal prismatic in 1T-TaS_2. Solid State Ion. *59*, 313–319.

42. Ding, Q., Song, B., Xu, P., and Jin, S. (2016). Efficient electrocatalytic and photoelectrochemical hydrogen generation using MoS_2 and related compounds. Chem *1*, 699–726.

43. Zeng, Z., Yin, Z., Huang, X., Li, H., He, Q., Lu, G., Boey, F., and Zhang, H. (2011). Single-layer semiconducting nanosheets: high-yield preparation and device fabrication. Angew. Chem. Int. Ed. *50*, 11093–11097.

44. Zeng, Z., Sun, T., Zhu, J., Huang, X., Yin, Z., Lu, G., Fan, Z., Yan, Q., Hng, H.H., and Zhang, H. (2012). An effective method for the fabrication of few-layer-thick inorganic nanosheets. Angew. Chem. Int. Ed. *51*, 9052–9056.

45. Fujita, T., Ito, Y., Tan, Y., Yamaguchi, H., Hojo, D., Hirata, A., Voiry, D., Chhowalla, M., and Chen, M. (2014). Chemically exfoliated ReS_2 nanosheets. Nanoscale *6*, 12458–12462.

46. Tsai, H.-L., Heising, J., Schindler, J.L., Kannewurf, C.R., and Kanatzidis, M.G. (1997). Exfoliated-restacked phase of WS_2. Chem. Mater. *9*, 879–882.

47. Zheng, J., Zhang, H., Dong, S., Liu, Y., Nai, C.T., Shin, H.S., Jeong, H.Y., Liu, B., and Loh, K.P. (2014). High yield exfoliation of two-dimensional chalcogenides using sodium naphthalenide. Nat. Commun. *5*, 2995.

48. Mahler, B., Hoepfner, V., Liao, K., and Ozin, G.A. (2014). Colloidal synthesis of 1T-WS_2 and 2H-WS_2 nanosheets: applications for photocatalytic hydrogen evolution. J. Am. Chem. Soc. *136*, 14121–14127.

49. Sun, Y., Wang, Y., Sun, D., Carvalho, B.R., Read, C.G., Lee, C.H., Lin, Z., Fujisawa, K., Robinson, J.A., and Crespi, V.H. (2016). Low-temperature solution synthesis of few-layer 1T′-$MoTe_2$ nanostructures exhibiting lattice compression. Angew. Chem. Int. Ed. *55*, 2830–2834.

50. Yin, Y., Zhang, Y., Gao, T., Yao, T., Zhang, X., Han, J., Wang, X., Zhang, Z., Xu, P., and Zhang, P. (2017). Synergistic phase and disorder engineering in 1T-$MoSe_2$ nanosheets for enhanced hydrogen-evolution reaction. Adv. Mater. *29*, 1700311.

51. Shi, J., Wang, X., Zhang, S., Xiao, L., Huan, Y., Gong, Y., Zhang, Z., Li, Y., Zhou, X., and Hong, M. (2017). Two-dimensional metallic tantalum disulfide as a hydrogen evolution catalyst. Nat. Commun. *8*, 958.

52. Cho, S., Kim, S., Kim, J.H., Zhao, J., Seok, J., Keum, D.H., Baik, J., Choe, D.H., Chang, K.J., and Suenaga, K. (2015). Phase patterning for ohmic homojunction contact in $MoTe_2$. Science *349*, 625–628.

53. Duerloo, K.A., Li, Y., and Reed, E.J. (2014). Structural phase transitions in two-dimensional Mo-and W-dichalcogenide monolayers. Nat. Commun. *5*, 4214.

54. Zhu, J., Wang, Z., Yu, H., Li, N., Zhang, J., Meng, J., Liao, M., Zhao, J., Lu, X., and Du, L. (2017). Argon plasma induced phase transition in monolayer MoS_2. J. Am. Chem. Soc. *139*, 10216–10219.

55. Ji, Q., Li, C., Wang, J., Niu, J., Gong, Y., Zhang, Z., Fang, Q., Zhang, Y., Shi, J., Liao, L., et al. (2017). Metallic vanadium disulfide nanosheets as a platform material for multifunctional electrode applications. Nano Lett. *17*, 4908–4916.

56. Lin, Y.C., Dumcenco, D.O., Huang, Y.S., and Suenaga, K. (2014). Atomic mechanism of the semiconducting-to-metallic phase transition in single-layered MoS_2. Nat. Nanotechnol. *9*, 391–396.

57. Kang, Y., Najmaei, S., Liu, Z., Bao, Y., Wang, Y., Zhu, X., Halas, N.J., Nordlander, P., Ajayan, P.M., and Lou, J. (2014). Plasmonic hot electron induced structural phase transition in a MoS_2 monolayer. Adv. Mater. *26*, 6467–6471.

58. Kan, M., Wang, J.Y., Li, X.W., Zhang, S.H., Li, Y.W., Kawazoe, Y., Sun, Q., and Jena, P. (2014). Structures and phase transition of a MoS_2 monolayer. J. Phys. Chem. C *118*, 1515–1522.

59. Johari, P., and Shenoy, V.B. (2012). Tuning the electronic properties of semiconducting transition metal dichalcogenides by applying mechanical strains. ACS Nano *6*, 5449–5456.

60. Enyashin, A.N., Yadgarov, L., Houben, L., Popov, I., Weidenbach, M., Tenne, R., Bar-Sadan, M., and Seifert, G. (2011). New route for stabilization of 1T-WS_2 and MoS_2 phases. J. Phys. Chem. C *115*, 24586–24591.

61. Li, H., Chen, S., Jia, X., Xu, B., Lin, H., Yang, H., Song, L., and Wang, X. (2017). Amorphous nickel-cobalt complexes hybridized with 1T-phase molybdenum disulfide via hydrazine-induced phase transformation for water splitting. Nat. Commun. *8*, 15377.

62. Liu, Q., Fang, Q., Chu, W., Wan, Y., Li, X., Xu, W., Habib, M., Tao, S., Zhou, Y., and Liu, D. (2017). Electron-doped 1T-MoS_2 via interface engineering for enhanced electrocatalytic hydrogen evolution. Chem. Mater. *29*, 4738–4744.

63. Xiang, T., Tao, S., Xu, W., Fang, Q., Wu, C., Liu, D., Zhou, Y., Khalil, A., Muhammad, Z., and Chu, W. (2017). Stable 1T-$MoSe_2$ and carbon nanotubes hybridized flexible film: binder-free and high-performance Li-ion anode. ACS Nano *11*, 6483–6491.

64. Hinnemann, B., Moses, P.G., Bonde, J., Jørgensen, K.P., Nielsen, J.H., Horch, S., Chorkendorff, I., and Nørskov, J.K. (2005). Biomimetic hydrogen evolution: MoS_2 nanoparticles as catalyst for hydrogen evolution. J. Am. Chem. Soc. *127*, 5308–5309.

65. Jaramillo, T.F., Jørgensen, K.P., Bonde, J., Nielsen, J.H., Horch, S., and Chorkendorff, I. (2007). Identification of active edge sites for electrochemical H_2 evolution from MoS_2 nanocatalysts. Science *317*, 100–102.

66. Fan, X.-L., Yang, Y., Xiao, P., and Lau, W.M. (2014). Site-specific catalytic activity in exfoliated MoS_2 single-layer polytypes for hydrogen evolution: basal plane and edges. J. Mater. Chem. A. *2*, 20545–20551.

67. Toh, R.J., Sofer, Z., Luxa, J., Sedmidubsky, D., and Pumera, M. (2017). 3R phase of MoS_2 and WS_2 outperforms the corresponding 2H phase for hydrogen evolution. Chem. Commun. *53*, 3054–3057.

68. Wang, H., Lu, Z., Xu, S., Kong, D., Cha, J.J., Zheng, G., Hsu, P.-C., Yan, K., Bradshaw, D., and Prinz, F.B. (2013). Electrochemical tuning of vertically aligned MoS_2 nanofilms and its application in improving hydrogen evolution reaction. Proc. Natl. Acad. Sci. USA *110*, 19701–19706.

69. Voiry, D., Fullon, R., Yang, J., de Carvalho castro E Silva, C., Kappera, R., Bozkurt, I., Kaplan, D., Lagos, M.J., Batson, P.E., and Gupta, G. (2016). The role of electronic coupling between substrate and 2D MoS_2 nanosheets in electrocatalytic production of hydrogen. Nat. Mater. *15*, 1003–1009.

70. Sasikumar, G., Ihm, J.W., and Ryu, H. (2004). Optimum Nafion content in PEM fuel cell electrodes. Electrochim. Acta *50*, 601–605.

71. Yin, Y., Han, J., Zhang, Y., Zhang, X., Xu, P., Yuan, Q., Samad, L., Wang, X., Wang, Y., and Zhang, Z. (2016). Contributions of phase, sulfur vacancies, and edges to the hydrogen evolution reaction catalytic activity of porous molybdenum disulfide nanosheets. J. Am. Chem. Soc. *138*, 7965–7972.

72. Tsai, C., Chan, K., Nørskov, J.K., and Abild-Pedersen, F. (2015). Rational design of MoS_2 catalysts: tuning the structure and activity via transition metal doping. Catal. Sci. Technol. *5*, 246–253.

73. Ambrosi, A., Sofer, Z., and Pumera, M. (2015). 2H→1T phase transition and hydrogen evolution activity of MoS_2, $MoSe_2$, WS_2 and WSe_2 strongly depends on the MX_2 composition. Chem. Commun. *51*, 8450–8453.

74. Deng, S., Zhong, Y., Zeng, Y., Wang, Y., Yao, Z., Yang, F., Lin, S., Wang, X., Lu, X., and Xia, X. (2017). Directional construction of vertical nitrogen-doped 1T-2H $MoSe_2$/graphene shell/core nanoflake arrays for efficient hydrogen evolution reaction. Adv. Mater. *29*, 1700748.

75. Seok, J., Lee, J.-H., Cho, S., Ji, B., Kim, H.W., Kwon, M., Kim, D., Kim, Y.-M., Oh, S.H., and Kim, S.W. (2017). Active hydrogen evolution through lattice distortion in metallic $MoTe_2$. 2D Mater. *4*, 025061.

76. Yuan, J., Wu, J., Hardy, W.J., Loya, P., Lou, M., Yang, Y., Najmaei, S., Jiang, M., Qin, F., and Keyshar, K. (2015). Facile synthesis of single crystal vanadium disulfide nanosheets by chemical vapor deposition for efficient hydrogen evolution reaction. Adv. Mater. *27*, 5605–5609.

77. Gopalakrishnan, D., Lee, A., Thangavel, N.K., and Arava, L.M.R. (2018). Facile synthesis of electrocatalytically active NbS_2 nanoflakes for an enhanced hydrogen evolution reaction (HER). Sustain. Energy Fuels *2*, 96–102.

78. Li, Y., Yu, Y., Huang, Y., Nielsen, R.A., Goddard, W.A., III, Li, Y., and Cao, L. (2014). Engineering the composition and crystallinity of molybdenum sulfide for high-performance electrocatalytic hydrogen evolution. ACS Catal. *5*, 448–455.

79. Yu, Y., Huang, S.-Y., Li, Y., Steinmann, S.N., Yang, W., and Cao, L. (2014). Layer-dependent electrocatalysis of MoS_2 for hydrogen evolution. Nano Lett. *14*, 553–558.

80. Parzinger, E., Mitterreiter, E., Stelzer, M., Kreupl, F., Ager, J.W., Holleitner, A.W., and Wurstbauer, U. (2017). Hydrogen evolution

activity of individual mono-, bi-, and few-layer MoS_2 towards photocatalysis. Appl. Mater. Today *8*, 132–140.

81. Sun, X., Dai, J., Guo, Y., Wu, C., Hu, F., Zhao, J., Zeng, X., and Xie, Y. (2014). Semimetallic molybdenum disulfide ultrathin nanosheets as an efficient electrocatalyst for hydrogen evolution. Nanoscale *6*, 8359–8367.

82. Chua, X.J., Luxa, J., Eng, A.Y.S., Tan, S.M., Sofer, Z.K., and Pumera, M. (2016). Negative electrocatalytic effects of p-doping niobium and tantalum on MoS_2 and WS_2 for the hydrogen evolution reaction and oxygen reduction reaction. ACS Catal. *6*, 5724–5734.

83. Tan, S.M., Sofer, Z.K., Luxa, J., and Pumera, M. (2016). Aromatic-exfoliated transition metal dichalcogenides: implications for inherent electrochemistry and hydrogen evolution. ACS Catal. *6*, 4594–4607.

84. Ambrosi, A., Sofer, Z., and Pumera, M. (2015). Lithium intercalation compound dramatically influences the electrochemical properties of exfoliated MoS_2. Small *11*, 605–612.

85. Latiff, N.M., Wang, L., Mayorga-Martinez, C.C., Sofer, Z., Fisher, A.C., and Pumera, M. (2016). Valence and oxide impurities in MoS_2 and WS_2 dramatically change their electrocatalytic activity towards proton reduction. Nanoscale *8*, 16752–16760.

86. Chen, X., and Wang, G. (2016). Tuning the hydrogen evolution activity of MS_2 (M = Mo or Nb) monolayers by strain engineering. Phys. Chem. Chem. Phys. *18*, 9388–9395.

87. Pan, H. (2014). Metal dichalcogenides monolayers: novel catalysts for electrochemical hydrogen production. Sci. Rep. *4*, 5348.

88. Abe, R. (2010). Recent progress on photocatalytic and photoelectrochemical water splitting under visible light irradiation. J. Photochem. Photobiol. C Photochem. Rev. *11*, 179–209.

89. Walter, M.G., Warren, E.L., McKone, J.R., Boettcher, S.W., Mi, Q., Santori, E.A., and Lewis, N.S. (2010). Solar water splitting cells. Chem. Rev. *110*, 6446–6473.

90. Chen, X., Shen, S., Guo, L., and Mao, S.S. (2010). Semiconductor-based photocatalytic hydrogen generation. Chem. Rev. *110*, 6503–6570.

91. Lin, H., and Wang, X. (2016). Epitaxy of radial high-energy-facetted ultrathin TiO_2 nanosheets onto nanowires for enhanced photoreactivities. Adv. Funct. Mater. *26*, 1580–1589.

92. Lin, H., Li, Y., Li, H., and Wang, X. (2017). Multi-node CdS hetero-nanowires grown with defect-rich oxygen-doped MoS_2 ultrathin nanosheets for efficient visible-light photocatalytic H_2 evolution. Nano Res. *10*, 1377–1392.

93. Hu, J.S., Ren, L.L., Guo, Y.G., Liang, H.P., Cao, A.M., Wan, L.J., and Bai, C.L. (2005). Mass production and high photocatalytic activity of ZnS nanoporous nanoparticles. Angew. Chem. Int. Ed. *117*, 1295–1299.

94. Ahmad, H., Kamarudin, S.K., Minggu, L.J., and Kassim, M. (2015). Hydrogen from photo-catalytic water splitting process: a review. Renew. Sust. Energ. Rev. *43*, 599–610.

95. Yang, J., Wang, D., Han, H., and Li, C. (2013). Roles of cocatalysts in photocatalysis and photoelectrocatalysis. Acc. Chem. Res. *46*, 1900–1909.

96. Du, H., Guo, H.-L., Liu, Y.-N., Xie, X., Liang, K., Zhou, X., Wang, X., and Xu, A.W. (2016). Metallic 1T-Li_xMoS_2 cocatalyst significantly enhanced the photocatalytic H_2 evolution over $Cd_{0.5}Zn_{0.5}S$ nanocrystals under visible light irradiation. ACS Appl. Mater. Interfaces *8*, 4023–4030.

97. Bai, S., Wang, L., Chen, X., Du, J., and Xiong, Y. (2015). Chemically exfoliated metallic MoS_2 nanosheets: a promising supporting co-catalyst for enhancing the photocatalytic performance of TiO_2 nanocrystals. Nano Res. *8*, 175–183.

98. Wang, L., Liu, X., Luo, J., Duan, X., Crittenden, J., Liu, C., Zhang, S., Pei, Y., Zeng, Y., and Duan, X. (2017). Self-optimization of the active site of molybdenum disulfide by an irreversible phase transition during photocatalytic hydrogen evolution. Angew. Chem. Int. Ed. *56*, 7610–7614.

99. Ding, Q., Meng, F., English, C.R., Cabán-Acevedo, M., Shearer, M.J., Liang, D., Daniel, A.S., Hamers, R.J., and Jin, S. (2014). Efficient photoelectrochemical hydrogen generation using heterostructures of Si and chemically exfoliated metallic MoS_2. J. Am. Chem. Soc. *136*, 8504–8507.